University of Texas Rio Grande Valley

ScholarWorks @ UTRGV

12-2005

Moving and stationary target acquisition radar image enhancement through polynomial windows

Rajarajeswari Devarajulu
University of Texas-Pan American

Recommended Citation

Moving and Stationary Target Acquisition Radar Image Enhancement through Polynomial Windows

A Thesis

by

RAJARAJESWARI DEVARAJULU

Submitted to the Graduate School of the
University of Texas-Pan American
In partial fulfillment of the requirement for the degree of

MASTER OF SCIENCE

December 2005

Major Subject: Electrical Engineering

Moving and Stationary Target Acquisition Radar Image Enhancement through Polynomial Windows

A Thesis
By
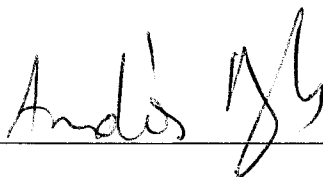RAJARAJESWARI DEVARAJULU

Approved as to style and content by:

Dr. Jae Sok Son, Ph.D
Assistant Professor, Electrical Engineering
Chair of Committee

Dr. Charles Harlow, Ph.D
Endowed Professor, Electrical Engineering
Committee Member

Dr. Andras Balogh, Ph.D
Associate Professor, Mathematics Department
Committee Member

December 2005

ABSTRACT

Devarajulu, Rajarajeswari, <u>Moving and Stationary Target Acquisition Radar Image Enhancement through Polynomial Windows</u>. Master of Science (MS), December 2005, 77 pp.; 3 tables, 39 figures, references, 42 titles.

The Fourier transform involved in synthetic aperture radar (SAR) imaging causes undesired sidelobes which obscure weak backscatters and affect the image clarity. These sidelobes can be suppressed without deteriorating the image resolution by smoothing functions known as windowing or apodization. Recently, the theory of orthogonal polynomials has gained considerable attention in signal processing applications. The window functions that are derived from the orthogonal polynomials have interesting sidelobe roll-off properties for better sidelobe apodization, hence it can be used for radar image enhancement.

In this work, a new window is constructed from Jacobi orthogonal polynomials and its performance in SAR imaging is analyzed and compared with commonly used window functions. Also, apodization functions involved in Fourier transform harmonic analysis and Fourier transform spectroscopy are discussed in the context of SAR imaging.

DEDICATION

I dedicate this thesis to my husband Dr. Sethu Subbarayalu and my parents for their

support.

ACKNOWLEDGEMENTS

I express my sincere thanks to my research advisor Dr. Jaesok Son for his invaluable support and encouragement provided during the course of my research work. I would like to thank Dr. Heinrich Foltz and Dr. Junfei Li for helping me to get this great opportunity.

I am also very thankful to my committee members, Dr. Charles Harlow and Dr. Andras Balogh, for insightful scientific discussions and for carefully examining the present manuscript. I am grateful to Dr. Mounir Ben Ghalia for his invaluable guidance throughout my research work.

I would like to thank Ms. Abby Tovar and Mr. Uriel Ramirez, who helped me throughout my course work. I would like to extend my gratitude to all my friends who made my stay at University of Texas Pan-American an enjoyable experience. Finally, I am grateful to National Geospatial-Intelligence Agency for supporting my research work.

TABLE OF CONTENTS

vii

LIST OF TABLES

LIST OF FIGURES

xi

CHAPTER 1

INTRODUCTION

1.1 Synthetic Aperture Radar

Synthetic aperture radar (SAR) is an airborne or satellite-borne radar system that provides high-resolution imaging. The SAR techniques rely on the motion of the radar systems relative to the target. The term synthetic aperture radar refers to a method of synthesizing a very large antenna by combining a series of signals received by the radar as it moves along its flight track.

It is possible for a SAR to penetrate through the places that infrared instruments cannot because of its longer wavelengths. Hence it is known as an excellent imaging tool that provides images in all weather conditions regardless of solar illumination. The SAR systems are a highly developed combination of precision hardware and electronic design for data acquisition, and advanced theoretical principles of mathematics and physics to convert the acquired data to high resolution images [1]. These synthetic aperture radars are broadly employed in environmental mapping, earth-resource mapping, and military systems that require wide-area imaging at high resolution.

1

1.2 Radar Imaging

Imaging radar functions similar to a flash camera that provides its own light to illuminate an area on the ground and take a picture at radar wavelengths. It uses an antenna and powerful digital signal processors to record the images instead of a camera lens and film of a flash camera [2].

For an example, European remote sensing satellite's (ERS-1) synthetic aperture radar transmits about 1700 high-power pulses per second toward the target or earth's surface. At the earth's surface the energy in the radar pulse is scattered in all directions and some reflected back towards the antenna. These backscatters or echoes are converted to digital data and processed further for display of the image. Figure 1.1 helps to understand the synthetic aperture radar imaging concept.
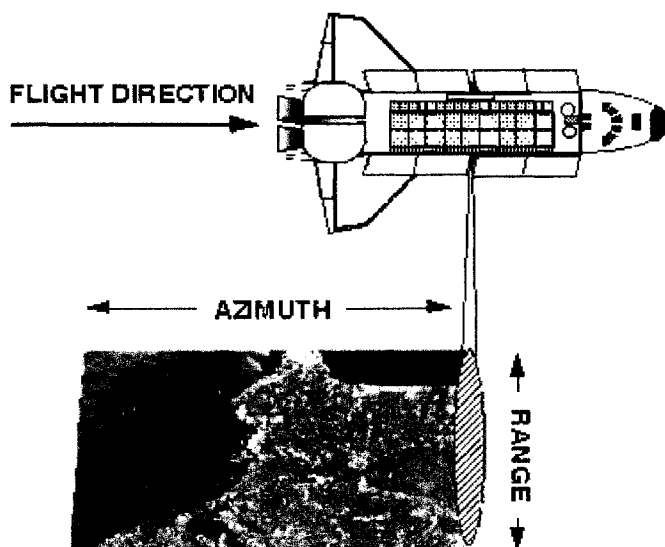
Figure 1.1 SAR imaging concept

The synthetic aperture radars produce two-dimensional images. One dimension in the image is called 'range' and is a measure of line-of-sight distance from the radar to the target [3]. The other dimension of the image is called 'azimuth' or along-track and is perpendicular to the radar range. The Range measurement and resolution are achieved in the synthetic aperture radar same as the conventional radars. Range resolution is given by

$$\nabla r = \frac{c}{2B}$$ (1)

where c is speed of light, and B is bandwidth of radar.

In traditional radars, a physically large antenna is needed to focus the transmitted and received energy into a sharp beam which defines the azimuth resolution. The synthetic aperture radars can collect data while flying and process the data as if it came from the physically large antenna. Hence the distance the aircraft flies in synthesizing the antenna is referred as synthetic aperture and it plays a major role in determining azimuth resolution of synthetic aperture radars. Azimuth resolution of SAR is given by

$$\nabla r_a = \frac{L}{2}$$ (2)

where L is length of radar antenna.

Achieving the azimuth resolution was also described from a Doppler processing point of view. The airborne radar transmits a pulse with the specific duration and center frequency. Because the radar is moving relative to the ground, the returned backscatters are Doppler shifted. The comparison of Doppler shifted frequencies to a reference frequency allows many returned signals to be focused on a single point. This focusing operation is commonly known as SAR processing. It requires precise knowledge of the relative motion between the platform and the

imaged objects, to correctly match the variation in Doppler frequency for each point in the image.

1.3 Fourier Transform in SAR imaging

Synthetic aperture radar transmits a sequence or burst of stepped frequency pulses towards the target at the ground. These bursts are reflected back to the radar at the earth's surface. The digital signal processor in the SAR helps to sample the received echoes and generates complex SAR data. In SAR signal history data, signal phase is more important than magnitude [4].

	Step 0	Step 1	Step	Step N-1		Range Cell 0	Range Cell 1	Range	Range Cell N-1
Burst 0	h(1,1)	h(1,2)		h(1,N)	DFT →	H(1,1)	H(1,2)		H(1,N)
.					DFT				
.									
.									
.					DFT				
Burst M-1	h(M,1)	h(M,2)	.....	h(M,N)	→	H(M,1)	H(M,2)	.....	H(M,N)

↓ IDFT   ↓ IDFT   ↓ IDFT

d(1,1)	d(1,2)		d(1,N)
d(M,1)	d(M,2)	.....	d(M,N)
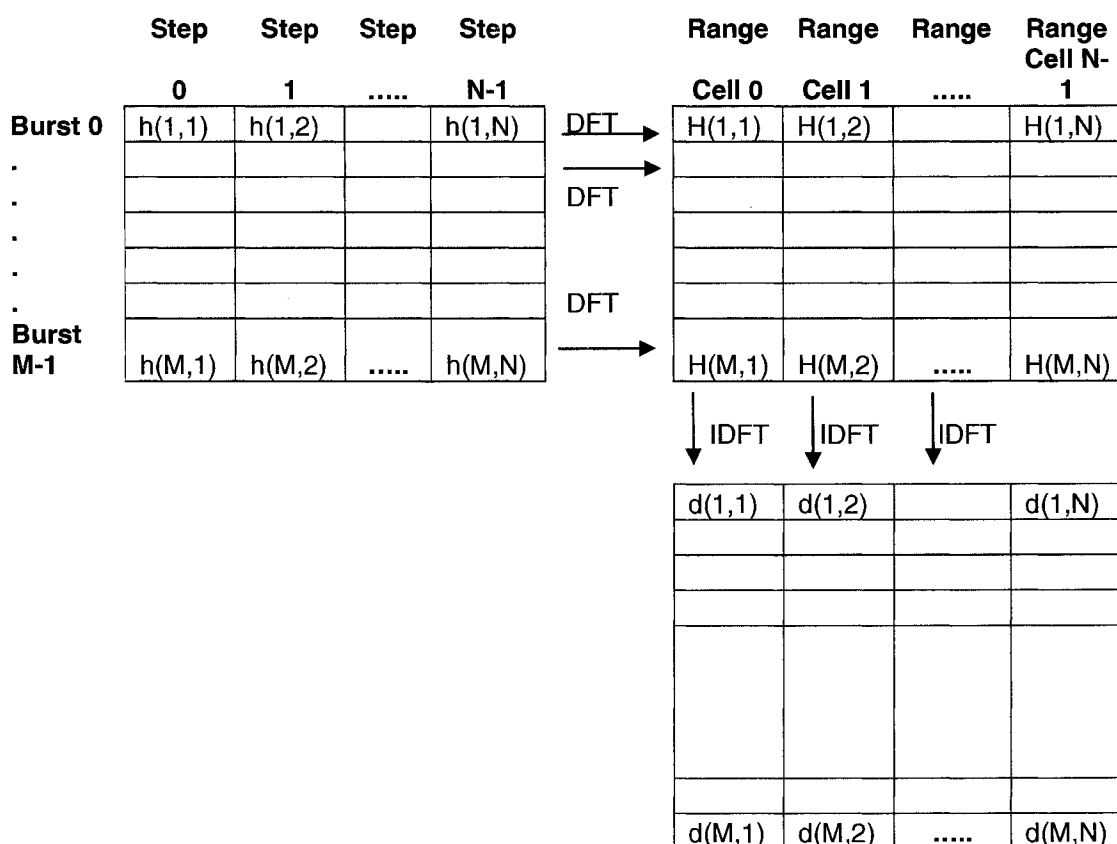
Figure 1.2 Image processing of SAR data

Figure 1.2 obtained from [5] helps to understand the formation of range profile and SAR image in a stepped-frequency SAR system. In the figure h (i, j) is the backscatter response from the ground at frequency f_j for burst i. In order to obtain the range profile first, the Fourier transform is applied row by row for the M bursts of N frequency samples. Then inverse Fourier transform is applied column by column. And the resulting matrix is referred to as SAR image matrix. Synthetic aperture radar images are composed of picture elements or pixels. Each pixel in the SAR image represents the radar backscatter for that area on the ground. The darker areas in the SAR image represent weak backscatter and brighter areas represent strong backscatter.

1.4 Gibb's Phenomenon

Fourier series is the representation of continuous-time periodic signals in terms of an infinite sum of complex exponentials [6]. The computation and study of Fourier series is known as harmonic analysis and is extremely helpful in decomposing a signal. In many engineering applications, the signals employed are periodic which lead naturally to a decomposition by a basis consisting of simple periodic functions. It is important that every observed signal we process must be of finite extent. The processing of finite-duration signals imposes interesting considerations in the harmonic analysis.

The problem involved with the Fourier series is referred to as Gibbs phenomenon. It was first observed by H. Wilbraham in 1848 and then analyzed in detail by Josiah W. Gibbs in 1899. The truncation of Fourier series caused discontinuities in time domain which lead to undesired oscillations in the frequency

domain. These undesired oscillations are called as ringing or sidelobes depending on

the applications. The Fourier series representation of a square signal is given by

$$s(t) = a_0 + \sum_{k=1}^{\infty} \left(a_k \cos\left(\frac{2\pi kt}{T}\right) \right) + \sum_{k=1}^{\infty} \left(b_k \sin\left(\frac{2\pi kt}{T}\right) \right) \tag{3}$$

Figure 1.3(a), Figure 1.3(b), and Figure 1.3(c) shows Fourier series approximation of

the square wave for various values of k.
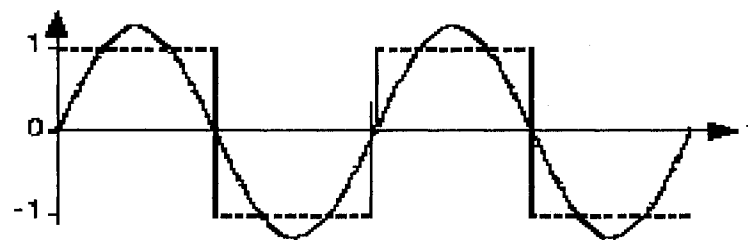
(a)

(b)

(c)

Figure 1.3 Gibbs Effect:

(a) k = 1 (b) k = 5 (c) k = 11

The SAR image is defined only on bounded domain referred as image window and it is assumed that the image is defined zero outside this window. So applying Fourier transform to the SAR image window is analogous to applying Fourier transform to a rectangular function. Figure 1.4(a) and Figure 1.4(b) shows the square wave and its corresponding Fourier transform.

(a)

(b)
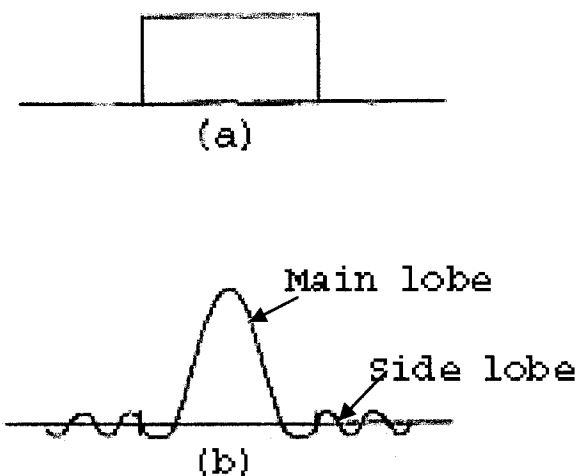
Figure 1.4 Fourier transform of a square function:
(a) Square function (b) Sinc function
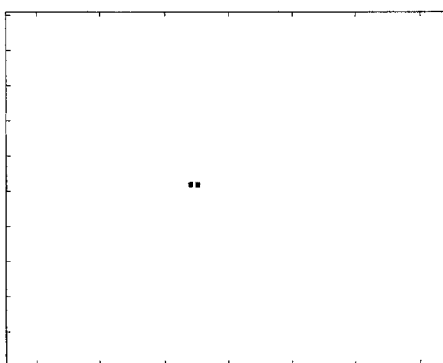
Figure 1.5 Fourier transform effect in two dimension image

Figure 1.5 shows the Fourier transform of a simulated two point targets obtained from [5]. It is obvious that sidelobes results due to Fourier transform and affects the image clarity.

1.5 Objectives of the Thesis

The Fourier transform involved in synthetic aperture radar image processing causes undesired sidelobes and obscures the resulting SAR images. The objective of this thesis is enhancing the SAR images by minimizing the sidelobes without compromising the mainlobe width. These sidelobes can be reduced by smoothing functions known as windows in signal processing and apodization in optics and radar imaging. In this work apodization functions involved in Fourier transform harmonic analysis and Fourier transform spectroscopy are discussed, and their performance in SAR imaging is compared. Recently the theory of orthogonal polynomials has gained considerable attention in signal processing applications because of its sidelobe roll-off properties. This sidelobe roll-off property helps to obtain better sidelobe pattern or sidelobe apodization. In this thesis, the use of orthogonal polynomials in SAR imaging is discussed and a new window is constructed from the Jacobi polynomials and applied first time for the SAR image enhancement.

1.6 Thesis Layout

The first chapter gives an introduction to the various concepts and terminologies relevant to the current work. Chapter two gives detailed description of various windowing techniques involved in harmonic analysis and analyzes their spectral characteristics. Chapter three introduces apodization functions involved in fourier transform spectroscopy. It also compares the performance of the apodization

functions discussed in chapters two and three. Chapter four explains the different types of apodization and analyzes their performance in SAR imaging. Chapter five discusses about the extrapolation techniques and their use in SAR imaging. Chapter six presents the formation of windows based on orthogonal polynomials. Chapter seven briefly addresses SAR image quality. Conclusion and future work are given in chapter eight.

CHAPTER 2

WINDOWING TECHNIQUE

Windowing is a process in which the data to be smoothed is multiplied by a window whose amplitude is maximum at the center and gradually decreases towards the edges. Over the last years, numerous investigators have proposed windows as different combinations of simple functions. The important factors that influence the choice of window functions are mainlobe width and sidelobe level. The sidelobe level helps to measure how well the windows suppress the spectral leakage and the mainlobe width is an indicator of the frequency resolution.

2.1 Windows in SAR Imaging

The window functions are well known in digital filter design and signal processing areas, where they are used to filter spatial or temporal data prior to spectral analysis in order to reduce the spectral leakage and loss of resolution. The two dimensional Fourier transform employed in SAR image processing results undesired spectral leakage known as sidelobes and affects the image clarity. The proper selection of windows helps to minimize these sidelobes and enhance the image. For a better SAR image enhancement the mainlobe width and the sidelobe height are maintained as small as possible.

10

Harris [7] discussed various window functions that satisfy optimality criteria for harmonic analysis. The windows such as rectangular, Hann, Hamming, and Blackman are referred to as classical fixed windows, in which the window length is the only parameter that controls the mainlobe width and the sidelobe levels. The window functions that used more than one parameter to control their spectral characteristics are referred to as adjustable windows. Each window with its own characteristics is selected based on specific applications. This chapter introduces different window functions that are used throughout this research and examines their spectral characteristics.

2.2 Rectangular Window

Rectangular window function known as uniform weighting is also referred to as Dirichlet window. The rectangular window is defined as

$$w_R(n) = 1, \quad |n| \leq \frac{N}{2}$$
$$= 0, \quad otherwise \tag{4}$$

where N is length of the window. This window function is Fourier transformed to obtain the spectral window. The Fourier transform of the rectangle window is a sinc function:

$$W_R(\omega) = N\left(\frac{\sin(\pi\omega N)}{\pi\omega N}\right)\exp^{-i\pi\omega N} \tag{5}$$

The spectral characteristics of the rectangle window for a window of length 31 are plotted in Figure 2.1. The window length is inversely proportional to the mainlobe width. The rectangle window has the narrowest mainlobe width that influences the image resolution. The main disadvantage of the rectangular window is its high sidelobe levels.
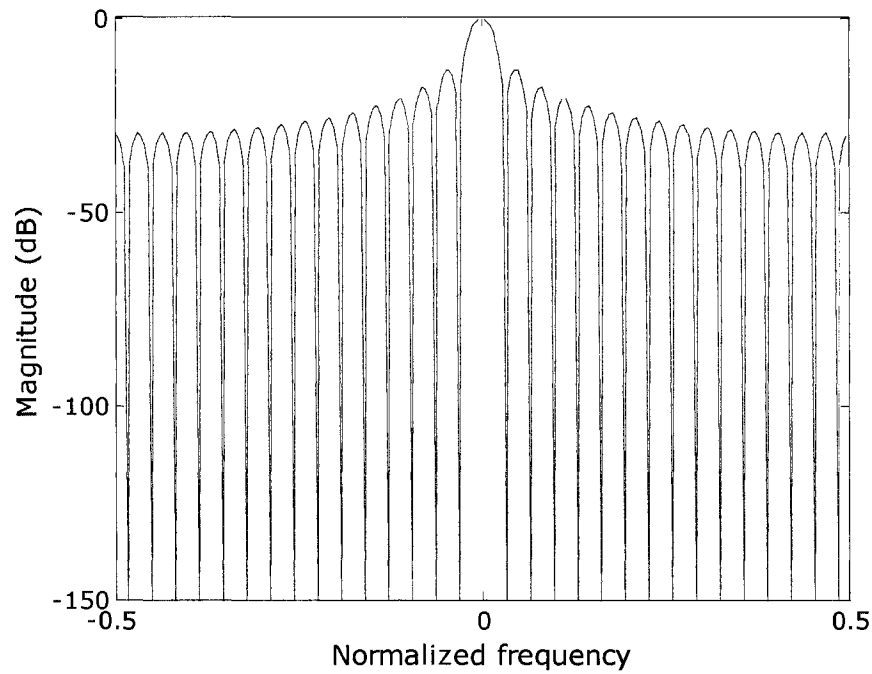
Figure 2.1 Spectral characteristics of rectangular window

2.3 Hann and Hamming Windows

Hann window was named after Julius Van Hann by R.B. Blackman and John Tukey in 1959. The Hann window is defined as

$$w_{hn}(n) = 0.5 + 0.5\cos\left(\frac{2n}{N}\pi\right), \quad |n| \leq \frac{N}{2} \tag{6}$$

The spectral characteristics of the Hann window are obtained by applying discrete Fourier transform to the Hann window function. Hamming window is obtained by Richard Wesley Hamming from the sum of the rectangular and the Hann window. The Hamming window is defined as

$$w_{h}(n) = 0.54 + 0.46\cos\left(\frac{2n}{N}\pi\right), \quad |n| \leq \frac{N}{2} \tag{7}$$

These windows are also referred to as cosine windows. Figure 2.2 shows the frequency responses of the Hann and Hamming windows for a window length 31.
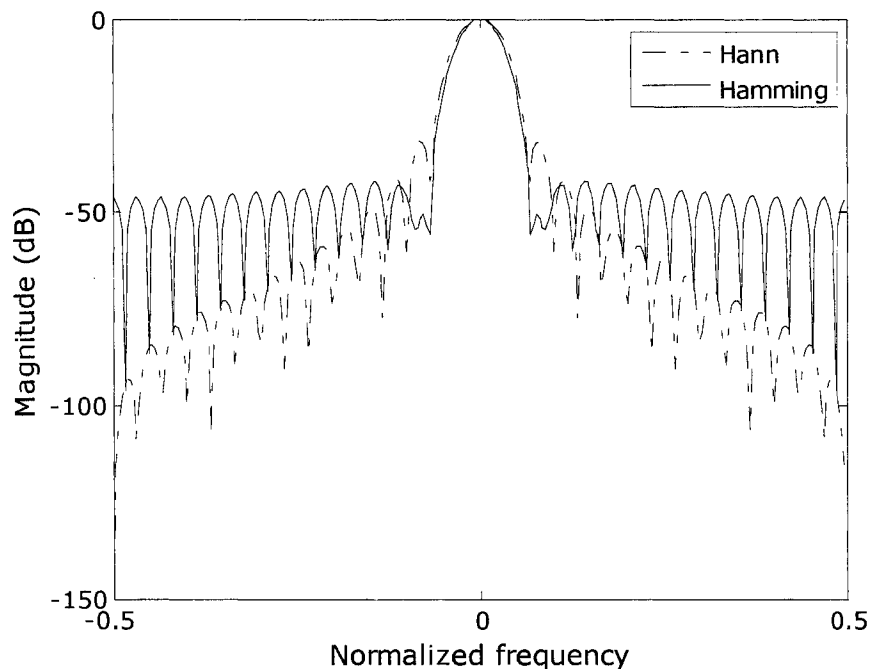
Figure 2.2 Spectral characteristics of Hann and Hamming windows

The Hann window controls the overall sidelobe levels effectively for the same mainlobe width than that of the Hamming window. But the Hamming window suppresses the first sidelobe level better compared to the Hann window. But the mainlobe becomes wider in these cosine windows.

2.4 Poisson, Gaussian and Cauchy Windows

The Gaussian window is defined as

$$w_{gauss}(n) = \exp\left[-\frac{1}{2}\left[\alpha\frac{n}{N/2}\right]^2\right], \qquad |n| \le \frac{N}{2} \tag{8}$$

where α is reciprocal of the standard deviation. The increase in α helps to decrease the sidelobe levels but increases the mainlobe width. The two sided exponential Poisson window is defined as

$$w_{poisson}(n) = \exp\left(-\alpha\frac{|n|}{N/2}\right), \qquad |n| \le \frac{N}{2} \tag{9}$$

The window characteristics vary depending on the α values similar to the Gaussian window. Cauchy window characteristics also depend on the parameter α. The Cauchy window function forms a two-sided exponential, when it is represented on a log scale. The window function is given by

$$w_{cauchy}(n) = \frac{1}{1 + \left[\alpha\frac{n}{N/2}\right]^2}, \qquad |n| \le \frac{N}{2} \tag{10}$$

The above windows are also referred as exponential windows. These exponential windows have two parameters to control the spectral characteristics. However, the increase in the parameter α reduces the sidelobe levels but the mainlobe becomes very wide and makes these windows unsuitable for practical applications. The spectral characteristics of the Gauss, Poisson and Cauchy windows are plotted in Figure 2.3 and Figure 2.4 for a window of length 31, and α values 2 and 3 respectively. These windows are also referred to as parametric windows [8].
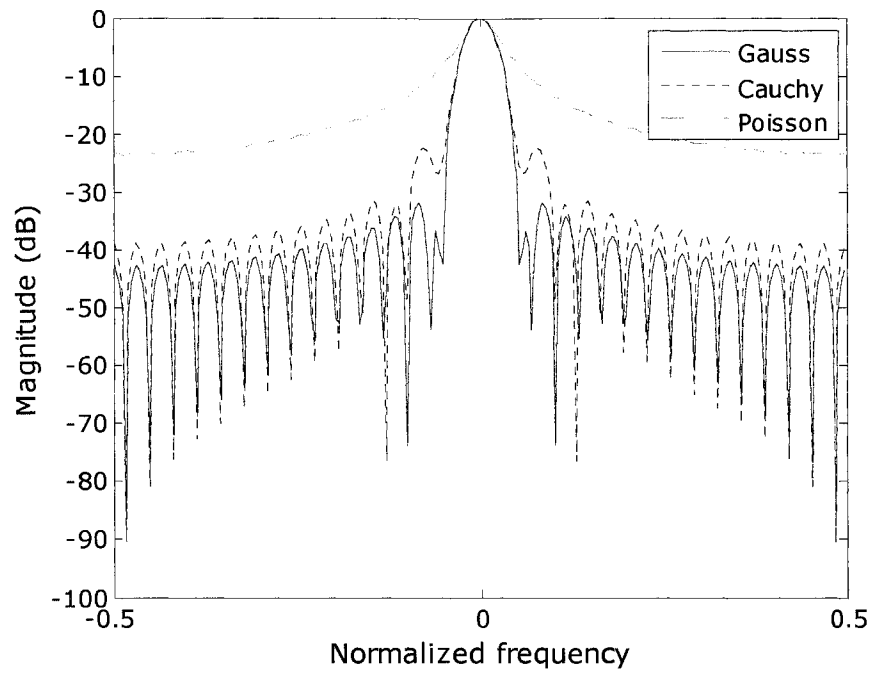
Figure 2.3 Spectral characteristics of exponential windows 1
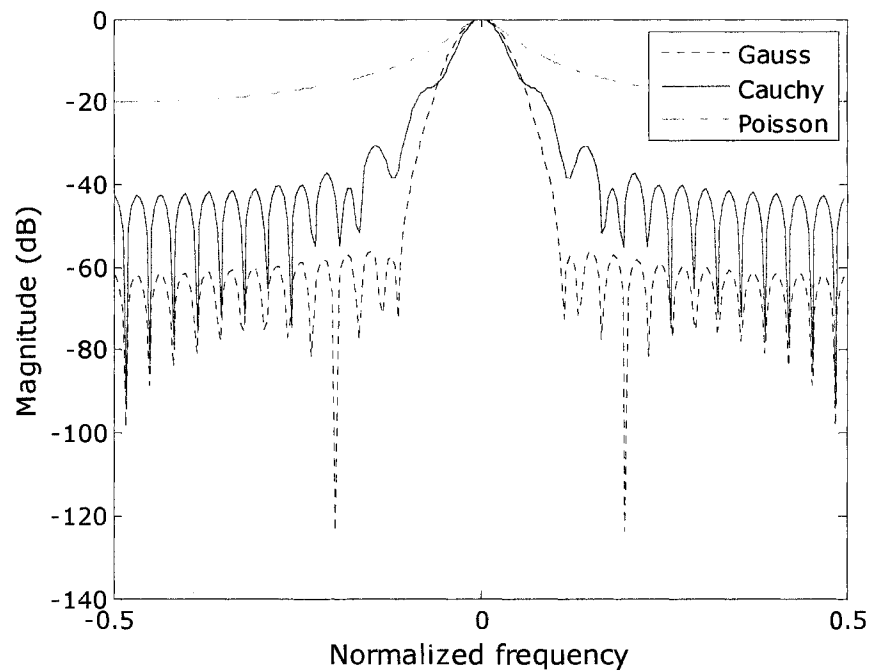
Figure 2.4 Spectral characteristics of exponential windows 2

2.5 Kaiser Window

Kaiser window is classified as an adjustable window because its window characteristics are controlled by window length and the parameter β. The Kaiser window is defined as [9]

$$w_k(n) = \frac{I_0\left[\pi\beta\sqrt{1-\left(\frac{n}{N/2}\right)^2}\right]}{I_0(\pi\beta)}, \qquad |n| \leq \frac{N}{2} \tag{11}$$

where $I_0(x)$ denotes the zero order modified Bessel function. Kaiser obtained the empirical relationship between the sidelobe attenuation levels (Att) and the β value:

$$\beta = \begin{cases} 0.1102(Att-8.7), & Att > 50 \\ 0.5842(Att-21)^{0.4} + 0.07886(Att-21), & 21 \leq Att \leq 50 \\ 0, & Att < 21 \end{cases} \tag{12}$$

The spectral characteristics of the Kaiser window for various β values are plotted in the figure 6. The increase in β slightly widens the mainlobe width but suppresses the siedlobe levels very well. Also, the Kaiser window has better sidelobe minimization than the Hann window for a slight increase in the mainlobe width. The Kaiser window is preferred for the harmonic analysis and many other applications because of its better trade off between the mainlobe width and the sidelobe level.
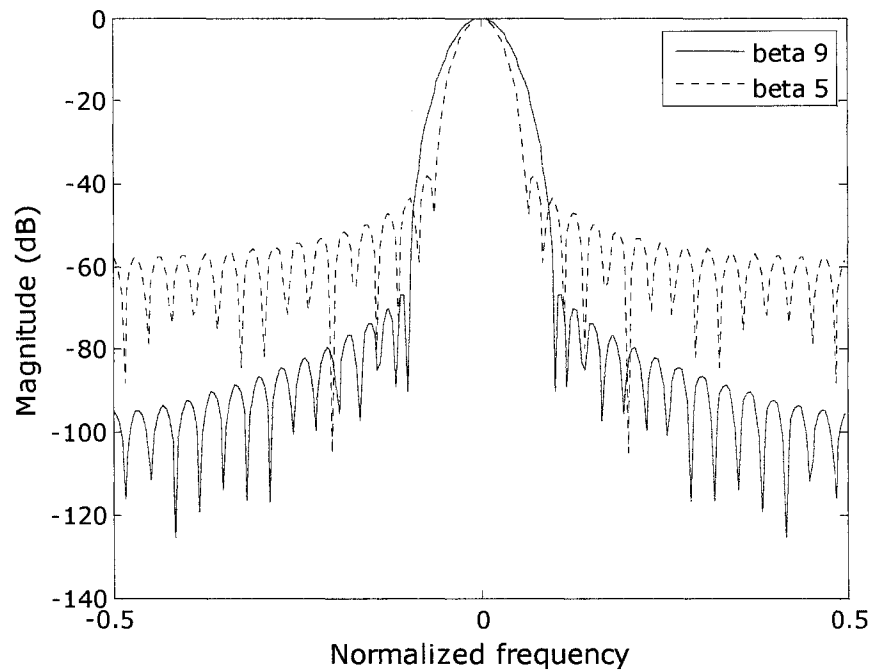
Figure 2.5 Spectral characteristics of Kaiser window

2.6 Windowing in Two Dimensions

Two dimensional implementation of window is a straight forward manner of one dimension. The Hann and Kaiser windows are applied to a simulated single point target and the resulting images are shown in Figure 2.6. Figure 2.6(a) show the original single point target image. Figure 2.6(b) and 2.6(c) show Hann and Kaiser windowed images of the simulated single point target respectively. The mainlobe width increases in Hann and Kaiser windowed images compared to the rectangular window image. The rectangular windowed image in Figure 2.6(b) shows more sidelobes compared to the other two windowed images.
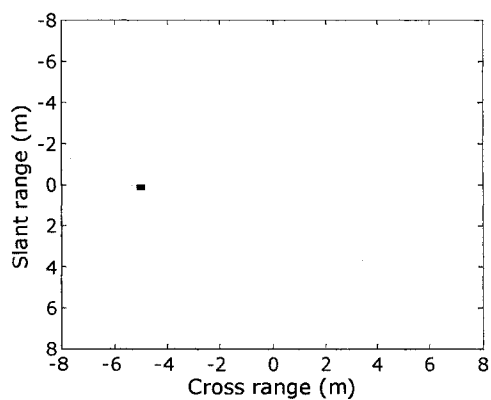
(a)
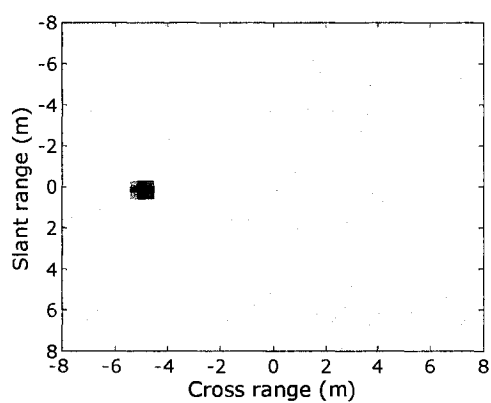
(b)
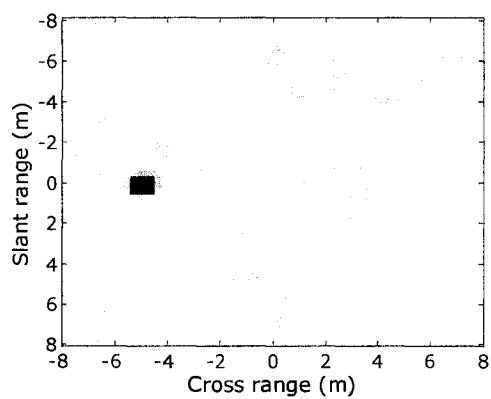
(c)

Figure 2.6 Windowing in simulated target:

(a) Original target (b) Hann window image (c) Kaiser window image
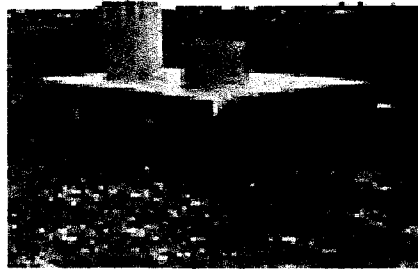
(a)
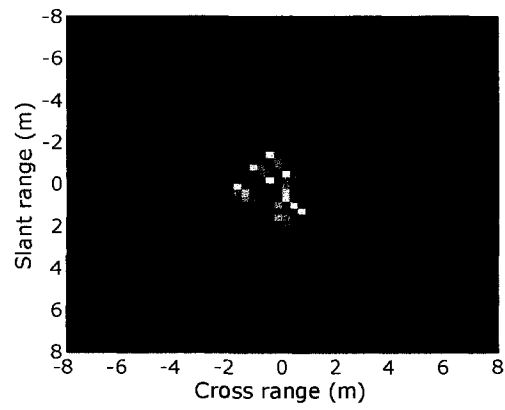
(b)
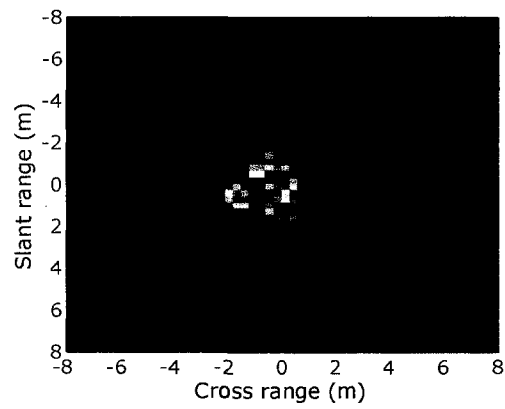
(c)
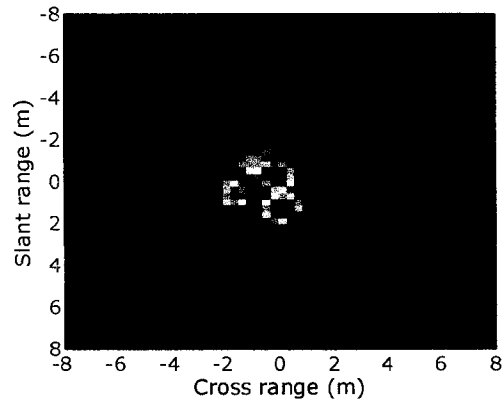
(d)

Figure 2.7 Windowing in two dimensions:

(a) Slicy image (b) Reference image (c) Hann image (d) Kaiser image

The Hann and Kaiser windows are applied to an image that is obtained from MSTAR data hb19377.015 and the resulting images are shown in Figure 2.7. The original picture of a target Slicy is shown in Figure 2.7(a). Figure 2.7(b) shows the original rectangular windowed image of the target Slicy and considered as a reference target image. Figure 2.7(c) and 2.7(d) show Hann and Kaiser windowed images of the Figure 2.7(a) respectively. Hann windowed image shows reduced sidelobes compared to the rectangular windowed image. Kaiser window suppresses sidelobes better among the three windows.

2.7 Discussion

Commonly used windows are analyzed in both one and two dimensions. The rectangular window shows the narrowest mainlobe width, but sidelobe levels are high and affect the SAR image clarity. The Kaiser windowed images clearly show the increase in the mainlobe width and better sidelobe reduction.

CHAPTER 3

APODIZATION

Apodization is a term often used in optics to refer the suppression of diffraction sidelobes [10]. It is widely used in synthetic aperture radar research because sidelobe control in SAR imaging is similar to sidelobe suppression in optics. Hence apodization is a technique used to reduce the sidelobes in optics and radar imaging applications, which results due to Fourier transform involvement in imaging process. Depending on the choice of an apodization function, the sidelobes are more or less suppressed and the image is more or less enhanced. This chapter briefly addresses imaging spectroscopy and discusses apodizaiton functions used in the imaging spectroscopy applications and compares them with the windows discussed in the chapter 2.

3.1 Imaging Spectroscopy

Spectroscopy is the study of light as a function of wavelength that has been emitted, reflected or scattered from a solid, liquid, or gas. The properties of light over a specific portion of the electromagnetic spectrum are measured by spectrometers. Fourier transform spectroscopy is a measurement technique whereby spectra are collected based on measurements of the temporal coherence of a radiative source, using time-domain measurements of the electromagnetic radiation or other type of radiation.

21

Imaging spectroscopy is a new technique for obtaining a spectrum in each position of a large array of spatial positions so that any one spectral wavelength can be used to make a recognizable image. It is a common practice to multiply the measured interferogram by an apodization function to reduce the amount of ringing present in the interferogram that obscure the interferogram resolution [11]. In 1950's astronomical applications started to use practical Fourier transform spectroscopy. Recently with the advances in computer and detector technology, the imaging spectroscopy technique is broadly employed in optical imaging applications.

3.2 Filler Apodization

Filler [12] developed two families of apodization functions to reduce the amount of ringing present in the interferogram. The Filler apodization functions are motivational force for Norton-Beer apodization functions [13]. The first family of Filler apodization is defined as

$$w_{fillerD}(n) = \frac{1}{1+\alpha}\left(\cos(\frac{\pi\rho}{2}) + \alpha\cos(\frac{3\pi\rho}{2})\right) \tag{13}$$

And the other family of filler apodization is defined as

$$w_{fillerE}(n) = \frac{1}{2+2\alpha}\left(1 + (1+\alpha)\cos(\pi\rho) + \alpha\cos(2\pi\rho)\right) \tag{14}$$

where ρ is related to the optical path difference and $0 < \alpha < 1$. For SAR imaging ρ is considered as $\frac{|n|}{N/2}$, where N is the length of the window and $|n| \le N/2$. In Figure 3.1 the spectral characteristics of Filler apodizations are plotted for a window of length 31 and α value 0.3.
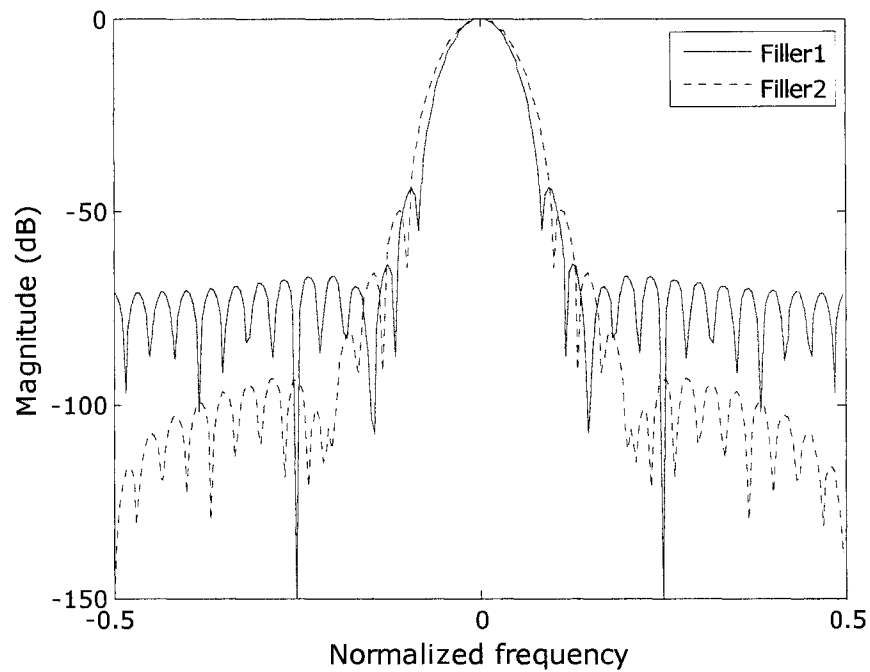
Figure 3.1 Spectral characteristics of Filler apodization

The first family of Filler apodization has narrower mainlobe width and few lower sidelobe levels but the second family of filler apodization has better trade-off between mainlobe width and sidelobe level. And Figure 3.2 compares the spectral characteristics of the Filler apodization against the Kaiser window. The Filler apodization has reduced over all sidelobe levels than the Kaiser window.
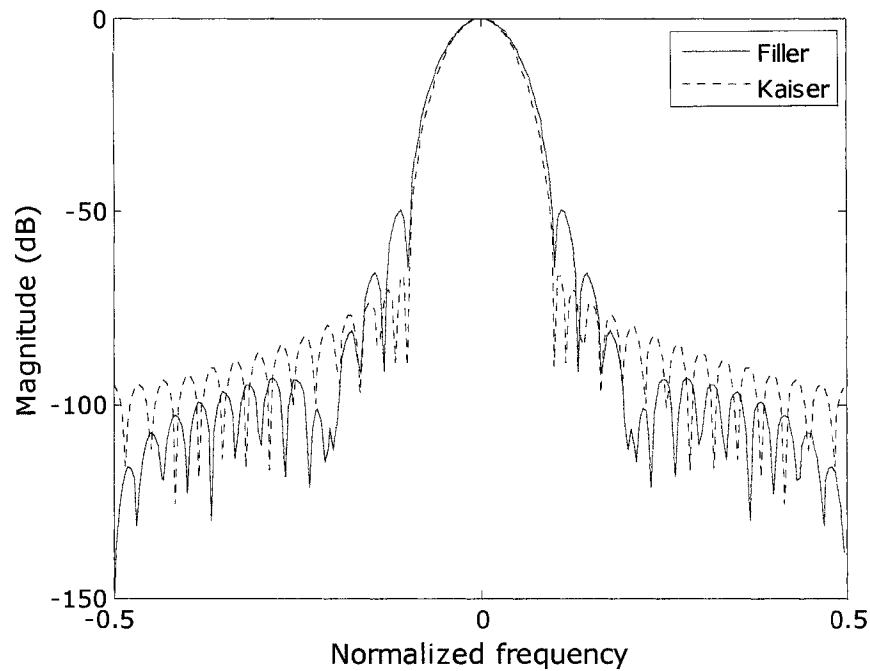
Figure 3.2 Comparison of Kaiser and Filler apodizations

3.3 Norton-Beer Apodization

Norton-Beer extended the Filler analysis and introduced three families of apodization functions: strong, medium and weak. The Norton-beer apodization functions are defined as

$$w_{norton1} = 0.548 - 0.0833(1 - \rho^2) + 0.5353(1 - \rho^2)^2$$
$$w_{norton2} = 0.26 - 0.154838(1 - \rho^2) + 0.0894838(1 - \rho^2)^2 \qquad (15)$$
$$w_{norton3} = 0.09 - 0.5875(1 - \rho^2)^2 + 0.3225(1 - \rho^2)^4$$

The first Norton-Beer apodization function minimizes the sidelobe level better than the other Norton-Beer apodization functions hence it is referred to as strong apodization. Figure 3.3 shows the performance of strong and medium Norton-Beer apodization functions. The Norton-Beer 1 minimizes sidelobes better than the Norton-Beer 2, hence called as strong Norton-Beer function.
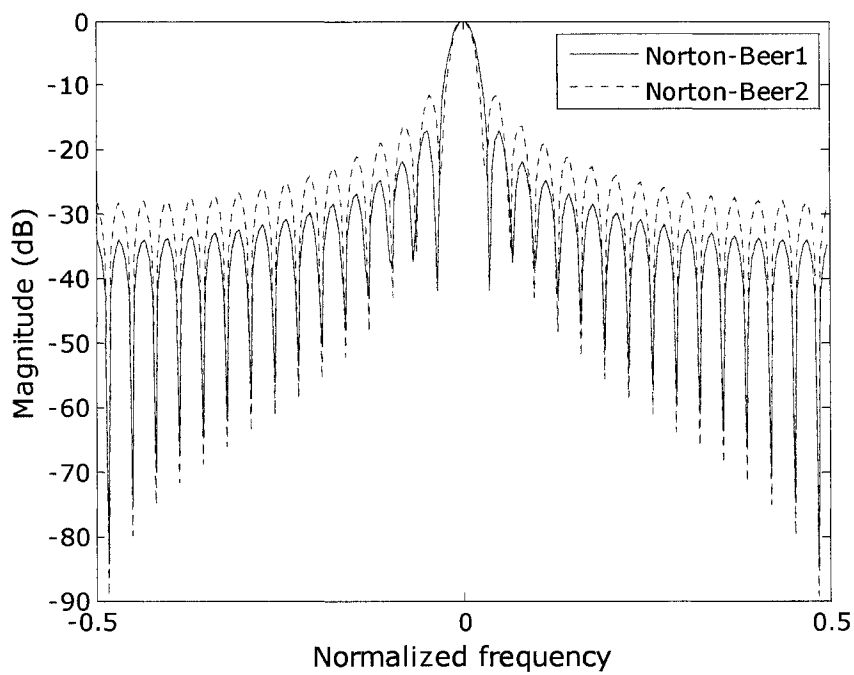
Figure 3.3 Spectral characteristics of Norton-Beer apodization
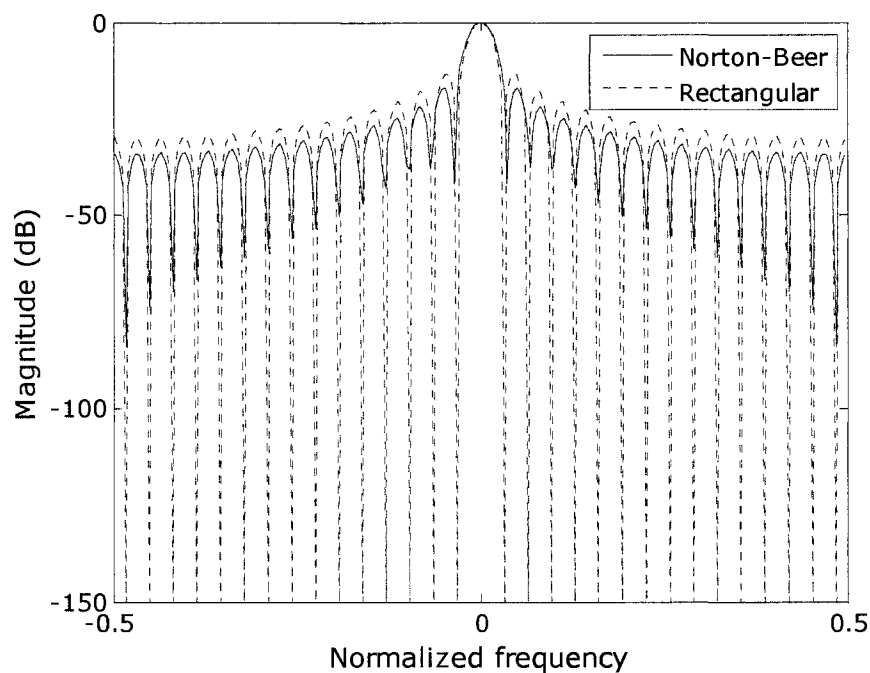
Figure 3.4 Comparison of Norton-Beer and rectangular apodizations

And Figure 3.4 compares the spectral characteristics of the Norton-Beer against the rectangular window. The Norton-Beer apodization has reduced sidelobe levels than the rectangular window.

3.4 Vander Mass Apodization

Vander Mass apodization [14] function is formed using Bessel functions similar to the Kaiser apodization. The Mass apodization is defined as

$$w_{mass} = \frac{I_1\left(\alpha\sqrt{1-\rho^2}\right)}{I_1(\alpha)\sqrt{1-\rho^2}}, \quad \alpha > 0$$

$$where \quad \rho = \frac{|n|}{N/2}, \quad |n| \le N/2 \tag{16}$$

where $I_1(x)$ denotes the modified bessel function of the first order and N is the length of the window. Figure 3.5 plots the spectral characteristics of the Mass window for a window length 31. The Mass apodization is compared against the Kaiser apodization because both the apodization developed based on the Bessel functions. The comparison of spectral characteristics in Figure 3.5 proves that the Kaiser window performs better than the Mass window. The Mass apodization has higher sidelobe levels than the Kaiser window.
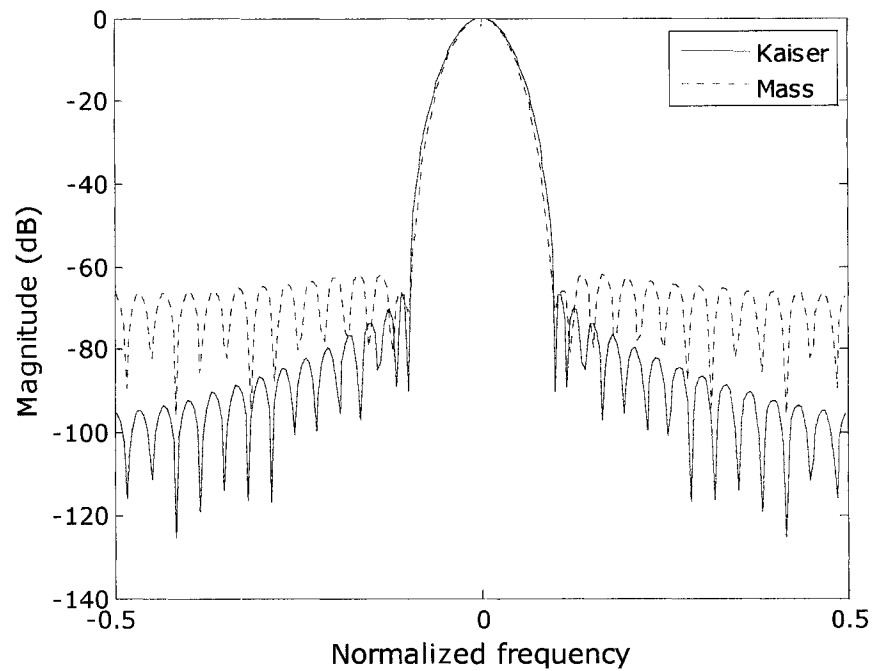
Figure 3.5 Spectral characteristics of Mass apodization

3.5 Apodization in Two Dimensions

Two dimensional implementation of apodization is similar to the two dimensional windows. The Filler and Norton-Beer apodizations are applied to an image that is obtained from MSTAR data hb19377.015 and the resulting images are shown in Figure 3.6. Figure 3.6(a) shows the original image of the MSTAR target Slicy. And Figure 3.6(b) shows its corresponding rectangular windowed SAR image. Figure 3.6(c) and 3.6(d) show Filler and Norton-Beer apodized images of the Figure 3.6(b).
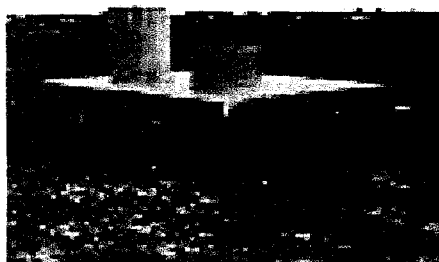
(a)
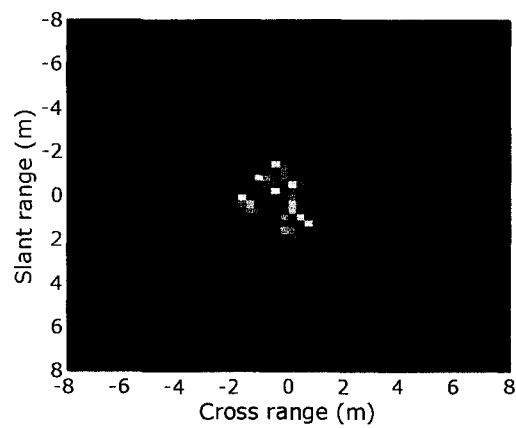
(b)
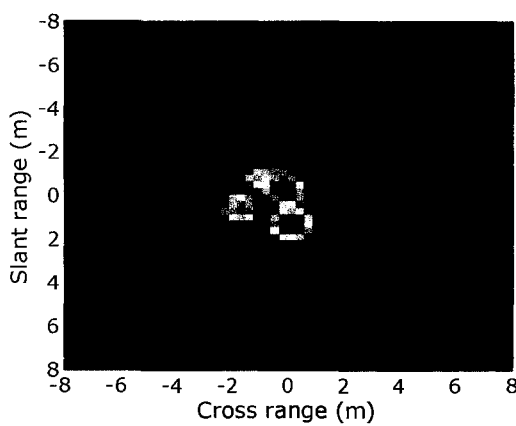
(c)
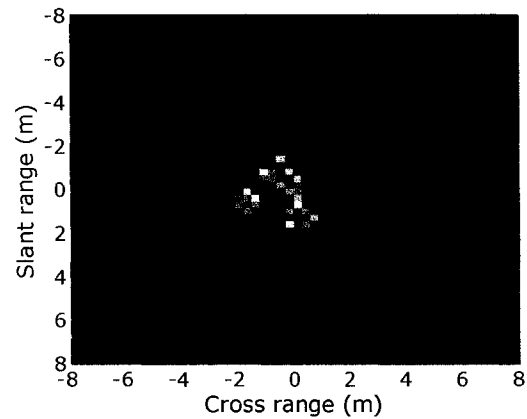
(d)

Figure 3.6 Apodization in two dimensions:

(a) Slicy picture (b) Reference image (c) Filler image (d) Norton-Beer image

3.6 Discussion

Apodization functions broadly employed in optics were analyzed in this chapter and applied for SAR image enhancement. Kaiser apodization developed from Bessel function of zero order shows better sidelobe reduction compared to the Mass apodization constructed from Bessel function of order one. Windows formed from Filler and Norton-Beer apodization show interesting spectral characteristics. The Filler image shows suppressed sidelobes, but increases the mainlobe width. The Norton-beer image reduces sidelobes compared to the rectangular windowed image without compromising the mainlobe width.

CHAPTER 4

APODIZATION TYPES

In general, one window function is used to minimize the sidelobes. Apodization types are developed by combining two or more window functions in different manner to obtain the better sidelobe and mainlobe control. This chapter introduces different apodization methodologies for enhancing the SAR images. The implementation is carried out in both one and two-dimensional manner.

4.1 Dual Apodization

In this method two different versions of windows or apodization functions are applied to the same input data. And at each spatial location the minimum value from the pair of windowed data is selected. Mostly dual apodization refers to the combination of uniform weighting or rectangular apodization with any other apodization function because the rectangular apodization has the narrowest mainlobe width compared to the other apodization functions.

Dual apodization makes a decision based only on the magnitude of the images. To utilize the complex values of the windowed data, first the two versions of the windows are obtained then at each spatial location the real components of the two versions are examined. If the real part of the two windowed data are opposite, zero value is selected otherwise the absolute minimum of the two values is selected.

30

The same procedure is repeated for the imaginary components of the images. The resulting output is called as complex dual apodization.

Complex dual apodization (CDA) minimizes sidelobes better than dual apodization (DA) in one dimensional case but it is less effective for two dimensional images [15]. Figure 4.1 shows the one dimensional dual adpoization outputs for a window of length 31. First dual apodization is obtained from the rectangular and the Hann windows, and then second dual apodization is obtained from the rectangular and the Kaiser windows.
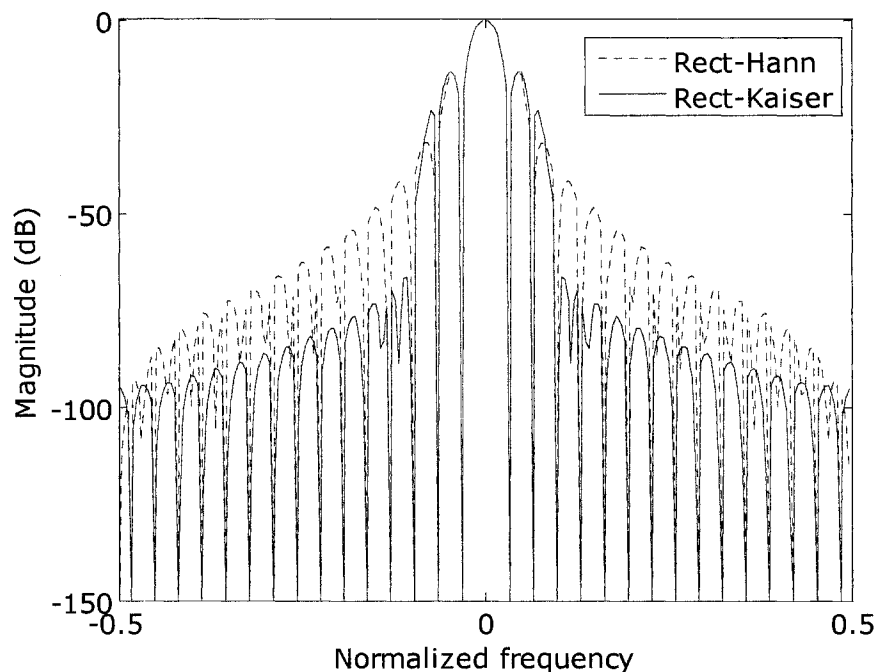
Figure 4.1 Dual apodization characteristics in one dimension

The Rect-Kaiser dual apodization suppresses sidelobes better than the Rect-Hann dual apodization. Both the apodizations have the same mainlobe width due to the rectangular window.
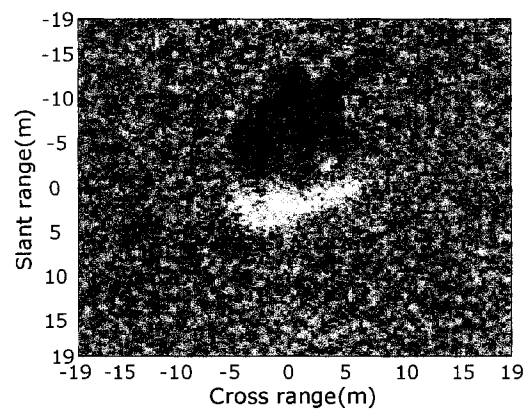
(a)
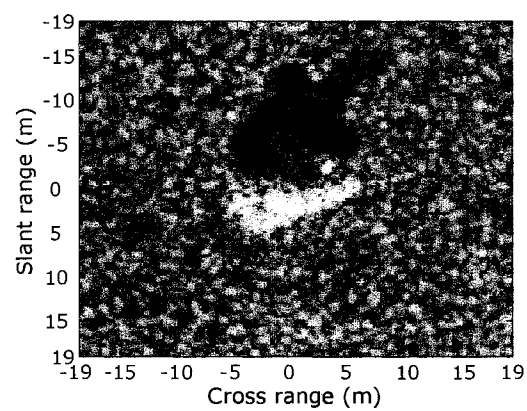
(b)
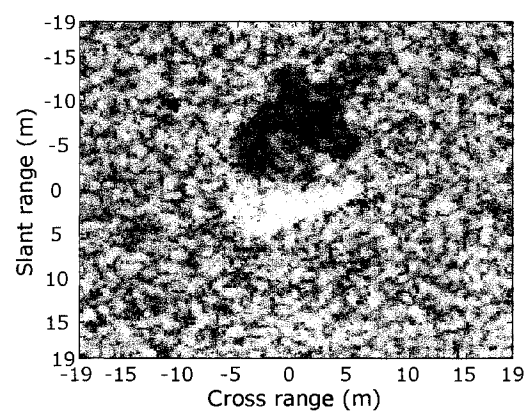
(c)

Figure 4.2 Dual apodization in two dimensions:

(a) Original image (b) Dual apodization 1 (c) Dual apodization 2

Figure 4.2(a) shows the original rectangular windowed image of the MSTAR target data HB03333.015. The first dual apodization image is from the rectangular and Hann windows and the second dual apodization image is from the rectangular and Kaiser windows, and the corresponding images are shown in Figure 4.2(b) and 4.2(c). The Figure 4.2(c) minimizes sidelobes better than the Figure 4.2(b).

4.2 Spatially Variant Apodization

Running multiple windows simultaneously for each sample and picking the best one adaptively as a function of neighboring data samples is referred to as spatially variant sidelobe apodization. In spatially variant apodization, the sidelobe minimization is achieved from a continuum of cosine-on-pedestal weighting functions.

Spatially variant apodization (SVA) effectively eliminates finite aperture induced sidelobes from uniformly weighted SAR data while retaining nearly all of the good mainlobe resolution [15, 16]. This is accomplished by taking the advantage of the special properties of raised-cosine weighting functions while dealing with sampled images.

The cosine-on pedestal weighting function is expressed as

$$A(n) = 1 + 2\omega\cos\left(2\pi\frac{n}{N}\right) \qquad (17)$$

This family of weighting function ranges from uniform weighting $(\omega = 0)$ to Hann weighting $(\omega = 0.5)$.

The discrete Fourier transform of the cosine-on-pedestal weighting function is defined as

$$a(m) = \omega\delta_{m,-1} + \delta_{m,0} + \omega\delta_{m,1} \qquad (18)$$

Where $\delta_{m,n}$ is the Kronecker delta function,

$$\delta_{m,n} = \begin{cases} 1, & m = n \\ 0, & m \neq n \end{cases} \tag{19}$$

Let us consider the original complex-valued image as

$$g(m) = I(m) + iQ(m) \tag{20}$$

Convolving the original image with the Fourier transformed cosine-on-pedestal weighting function yields the filtered image

$$g^{'}(m) = \omega(m)g(m-1) + g(m) + \omega(m)g(m+1) \tag{21}$$

where ω varies with respect to m, and can be chosen by minimizing $\left| g^{'}(m) \right|^2$.

$$\left| g^{'}(m) \right|^2 = [I(m) + w(m)\{I(m-1) + I(m+1)\}]^2 + \\ [Q(m) + w(m)\{Q(m-1) + Q(m+1)\}]^2 \tag{22}$$

By calculating the partial derivative of $\left| g^{'}(m) \right|^2$ and setting it equal to zero, we can obtain $\omega(m)$:

$$w(m) = -\frac{\{I(m)[I(m-1) + I(m+1)] + Q(m)[Q(m-1) + Q(m+1)]\}}{[I(m-1) + I(m+1)]^2 + [Q(m-1) + Q(m+1)]^2} \tag{23}$$

As we know, the weighting function lies between 0 to 0.5, the final output has the form

$$g^{'}(m) = \begin{cases} g(m), & w(m) < 0 \\ g(m) + w(m)[g(m-1) + g(m+1)], & 0 \leq w(m) \leq \frac{1}{2} \\ g(m) + \frac{1}{2}[g(m-1) + g(m+1)], & w(m) > \frac{1}{2} \end{cases} \tag{24}$$

The two dimensional implementation of SVA proceeds in a straightforward manner of one dimensional method. In modified SVA [17], the apodization technique is applied separately to the real and imaginary components of the image. It provides better image enhancement than the SVA applied to joint real and imaginary components of the image.
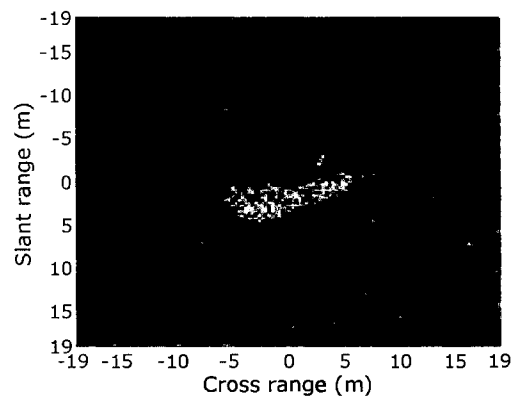
(a)
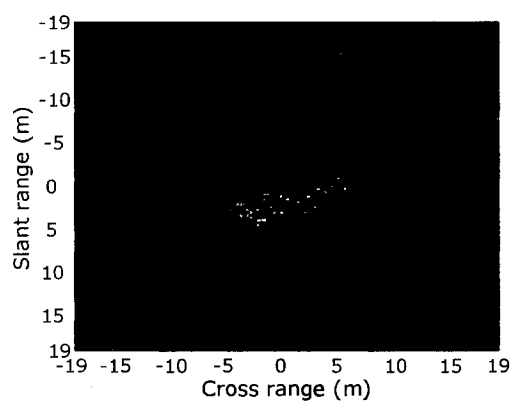
(b)
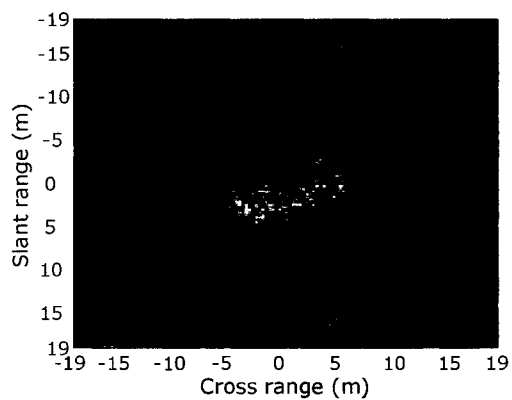
(c)

Figure 4.3 SVA results of MSTAR data 1:

(a) Original image (b) SVA image (c) Modified SVA image

Figure 4.3(a) shows the original rectangular windowed image of the MSTAR data HB03333.015. And Figure 4.3(b) and 4.3(c) show the corresponding SVA and modified SVA output images respectively.

4.3 Magnitude Difference Method

This method was proposed by Son [18] for SAR image enhancement. This method can also be referred to as modified dual apodization. The steps involved in modified dual apodization:

1. The data to be smoothed is multiplied by the rectangular and the Hann window, and the absolute difference between the two windowed data is calculated.

2. The difference data is subtracted from the rectangular windowed data.

3. The absolute rectangular windowed data is added with the absolute Hann widowed data and the resulting data is subtracted from the rectangular windowed data.

4. The data's obtained from the step 2 and 3 are maintained to the same value if the values are greater than zero.

5. The final data is obtained from the two data's of step 4 similar to the dual apodization.
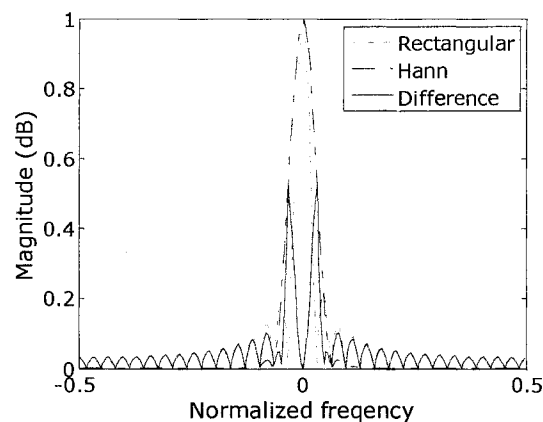
(a)
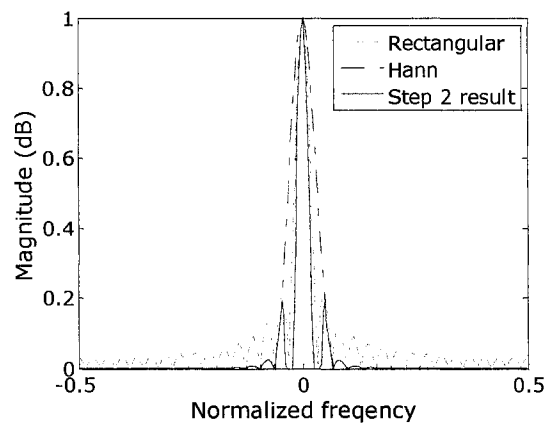
(b)
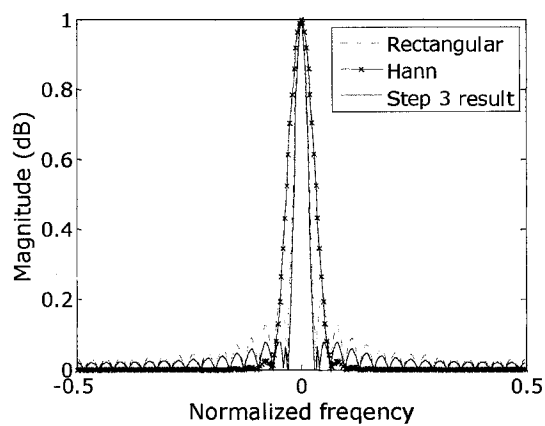
(c)
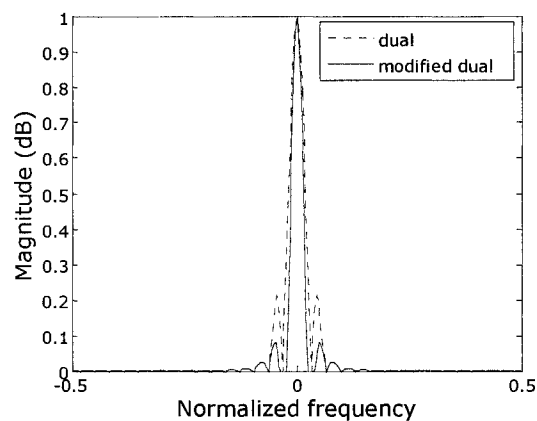
(d)

Figure 4.4 Modified dual apodization in one dimension:

(a) Difference output (b) Step 2 result (c) Step 3 result (d) Apodized output

Figure 4.4(a) shows the absolute difference between the rectangular and the Hann window. Figure 4.4(b) and Figure 4.4(c) shows the results of step 2 and 3 respectively. And Figure 4.4(d) shows the modified dual apodization output. Figure 4.5(a) and Figure 4.5(b) shows the original rectangular windowed image of a MSTAR data HB03333.015 and its corresponding apodized image respectively. The data manipulation is done based on [19, 20] and explained in the Appendices.
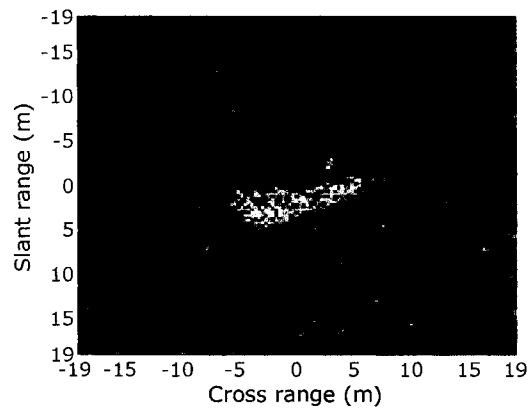
(a)
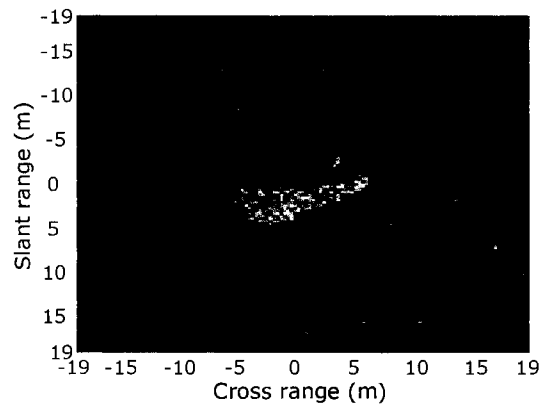
(b)

Figure 4.5 Modified dual apodization in two dimensions:
(a) Original image (b) Modified dual apodization image

4.4 Discussion

Apodization types are analyzed in this chapter. The results show that the modified dual apodization minimizes the sidelobe levels better than that of the dual apodization. But the dual apodization technique is not practically applicable becuase it makes decision based only on the magnitude of images. SVA suppresses sidelobes without compromising mainlobe width. But it is efficiently implemented as a three point convolution. This implementation requires that the data to be sampled at integer Nyquist rate. If the incoming data is sampled at a non-integer Nyquist rate, then the data must be upsampled to an integer rate, a process that increases the data storage requirements and processing time [42]. Also non-integer SVA may eliminate the backscatters that have weak amplitudes. Hence SVA is not suitable for all radar imaging applications.

CHAPTER 5

EXTRAPOLATION TECHNIQUES

The goal of extrapolation is to estimate the unknown values beyond the limit of a signal. The algorithms that help to estimate the frequencies beyond the image pass-band are also referred to as super-resolution algorithms. In general super-resolution is a technique that enhances the resolution of an imaging system. The super-resolution techniques [21] are widely employed in optics and radar imaging to improve the image resolution. This chapter discusses about the various extrapolation techniques and their role in SAR imaging.

5.1 Papoulis Extrapolation

Papoulis [22] developed an algorithm for extrapolating band-limited signals based on Gerchberg's [23] error energy reduction method. The known segment is considered as duration-limited portion of an original signal and given by

$$g(t) = f(t)p(t) \tag{25}$$

where

$$p(t) = \begin{cases} 1, & |T| \\ 0, & elsewhere \end{cases} \tag{26}$$

The function $f(t)$ is an original band-limited signal. If its energy E is finite and its transform $F(w)$ is zero outside a finite interval:

$$F(w) = 0, \qquad |w| > \Omega \tag{17}$$

Steps involved in Papoulis extrapolation algorithm:

40

1. Fourier Transform the known segment.

2. Multiply the Fourier transformed segment with the rectangular window.

3. Apply Inverse Fourier Transform.

4. Replace the known part of the signal.

The extrapolation procedure has been applied to the signal

$$f(t) = \sin\frac{\Omega t}{\pi t} \qquad (28)$$

T is chosen as $\Pi/5\Omega$. The extrapolation procedure is shown in Figure 5.1. Figure 5.1(b) is a duration limited signal selected from the given input signal shown in Figure 5.1(a). Figure 5.1(c) shows the resulting extrapolated signal. The extrapolation procedure applied to real MSTAR targets, and the resulting two dimensional extrapolated images are shown in Figure 5.2(c) .Figure 5.2(a) and shows the original images of the MSTAR targets SLICY and Figure 5.2(b) shows its corresponding rectangular windowed SAR image. The extrapolated image obscures the image clarity.
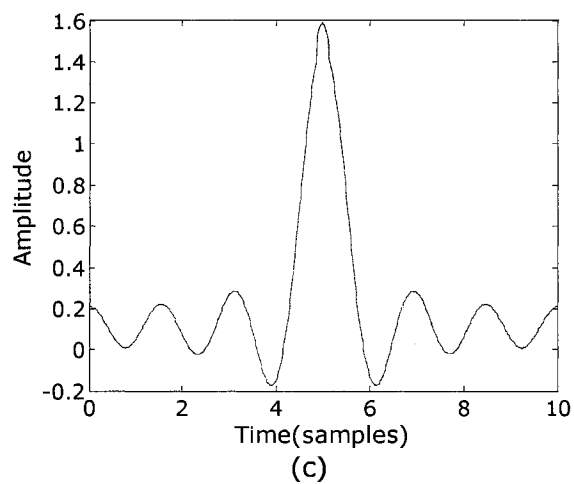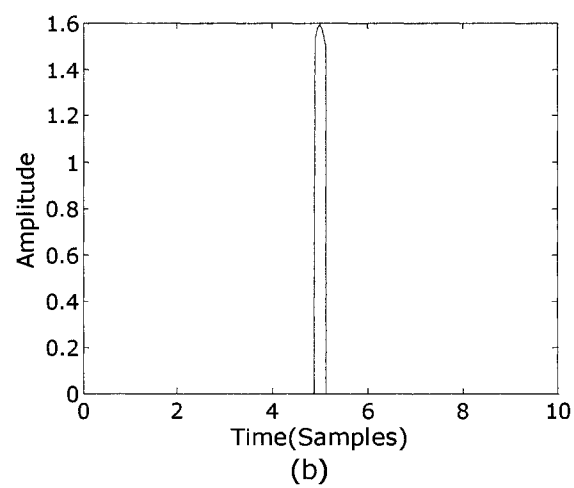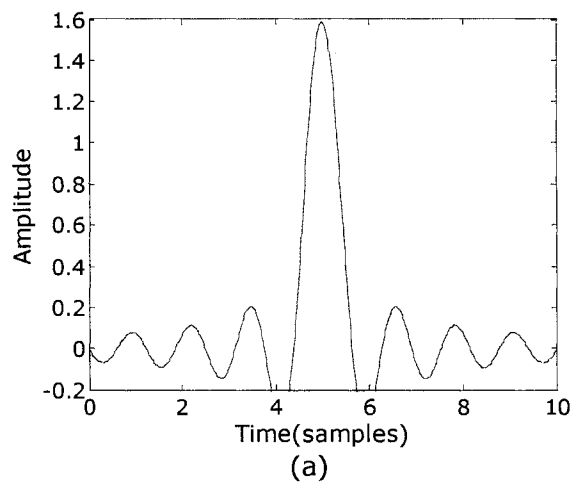
Figure 5.1 Extrapolation in one dimension:

(a) Input signal (b) Duration limited signal (c) Extrapolated signal
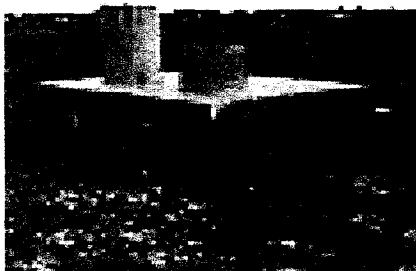
(a)
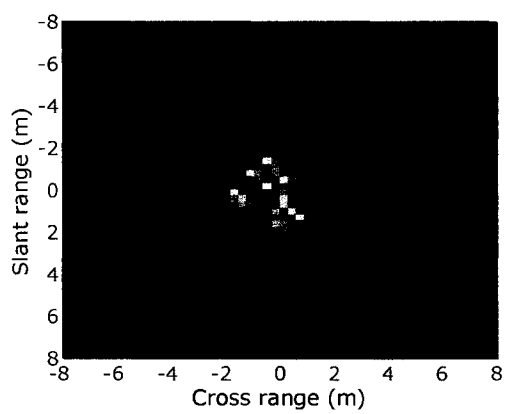
(b)
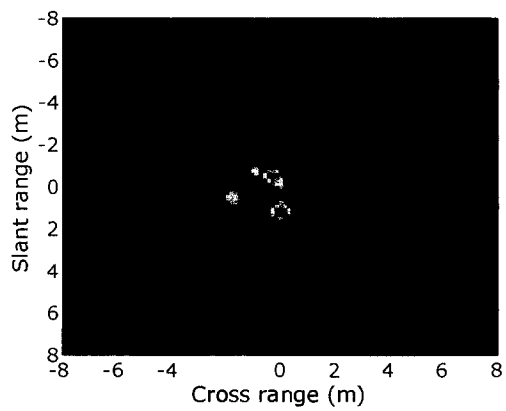
(c)

Figure 5.2 Extrapolation of MSTAR data 1:

(a) Slicy Picture (b) Rectangular windowed image (c) Extrapolated image

5.2 Extrapolation Matrix

To improve the convergence of Papoulis extrapolation, Sabri-Steenaart [24] replaced the number of iteration steps by a single extrapolation matrix.

The extrapolated signal results from this method is expressed in the following way,

$$g_n(t) = g_0(t) + Hg_0(t) + H^2 g_0(t) + \ldots + H^n g_0(t) \tag{29}$$

where g_0 is a signal to be extrapolated. And H is given as

$$H = DB \tag{30}$$

where D is duration limiting operator and B is band-limiting operator. The extrapolation matrix can be formed from the equation 35 as

$$E_n = \sum_{i=0}^{n} H^i \tag{31}$$

It provides faster convergence than the Papoulis method. But when the size of the input data increases, the extrapolation matrix becomes ill-conditioned, and becomes unsuitable for practical applications.

5.3 Minimum Norm Least Square Extrapolation

Minimum norm least square extrapolation was proposed by Jain [25] for band-limited discrete signals and it showed that the continuous extrapolation algorithms can be converted to discrete extrapolation algorithms. The minimum norm extrapolated signal is defined as

$$g^+ = BD^T (DBD^T)^{-1} g_0 \tag{32}$$
$$E^+ = BD(DBD^T)^{-1} \tag{33}$$

where E^+ is referred to as the pseudo-inverse extrapolation matrix. This matrix helps to avoid the ill-conditioning problem in the extrapolation matrix method.

Cabrera and Parks [26] introduced improved adaptive weighted norm extrapolation that does not restrict bandwidth based on the minimum norm least square method.

5.4 Super-SVA

Processes that achieve the recreation of frequencies beyond the image pass-band are generally referred as super-resolution algorithms. Super-SVA was proposed and demonstrated by Stankwitz et al [27], and later employed in SAR/ISAR image enhancement applications [28, 29]. The basic idea of Super-SVA is based on spatially variant apodization (SVA) and Papoulis extrapolation technique

The steps involved in Super-SVA:

1. Band limited data is considered as input.

2. Fourier transform applied to zeropadded input data.

3. Spatially Variant apodization used to smooth the spectral leakage results from fourier transform.

4. Inverse filtering performed.

5. The original input data is replaced in the center of the inverse filtered data.

6. And, the steps 2, 3, 4 & 5 repeated to obtain extrapolated data.

```
┌─────────────────┐
│   Input Data    │
└────────┬────────┘
         ▼
      ( FFT )◄──────────┐
         │              │
         ▼              │
┌─────────────────┐     │
│      SVA        │     │
└────────┬────────┘     │
         ▼              │
      ( FFT )           │
         │              │
         ▼              │
┌─────────────────┐     │
│ Data Replacement│     │
└────────┬────────┘     │
         ▼              │
┌─────────────────┐     │
│ Error Estimation│     │
└────────┬────────┘     │
         ▼          No  │
        ╱ Error ╲───────┘
        ╲Tolerance╱
         │ Yes
         ▼
┌─────────────────┐
│Extrapolated Output│
└────────┬────────┘
         ▼
┌─────────────────┐
│  Image Display  │
└─────────────────┘
```
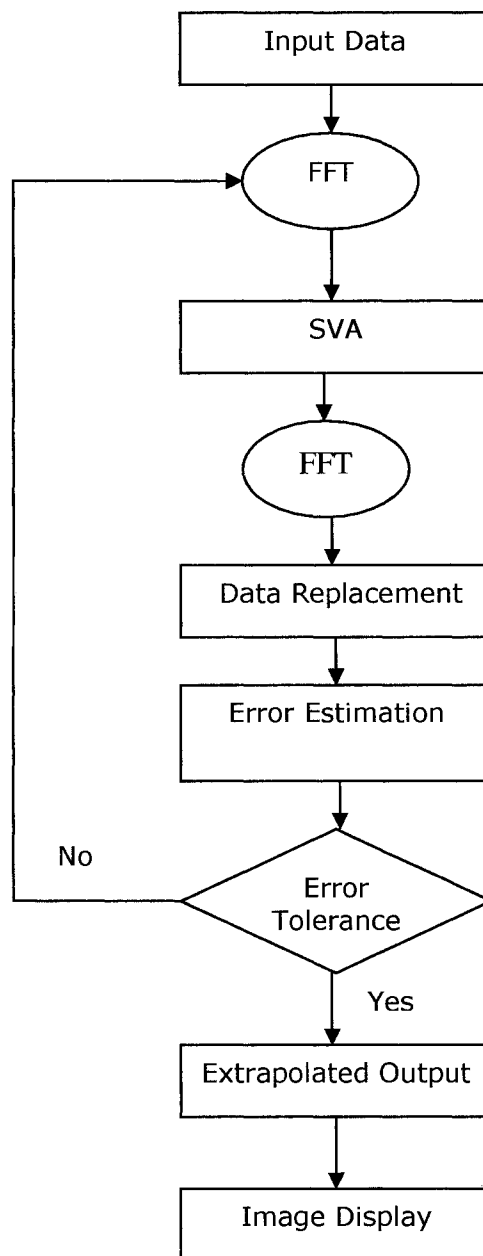
Figure 5.3 Block diagram of Super-SVA

Figure 5.3 shows the block diagram of Super-SVA. The one dimensional super-SVA results adapted from [27] is shown in Figure 5.4. Figure 5.4(a) shows a band limited input signal selected for Super-SVA technique. The Fourier transformed sinc function is shown in Figure 5.4(b). Figure 5.4(c) and 5.4(d) show the resulting SVA and

inverse filtered outputs respectively. And Figure 5.4(e) and 5.4(f) show the extrapolated output and its corresponding frequency response. The steps 2, 3, 4, and 5 are repeated to get the better result. The narrow mainlobe width of extrapolated frequency response shows that Super-SVA algorithm performs better than the SVA technique.
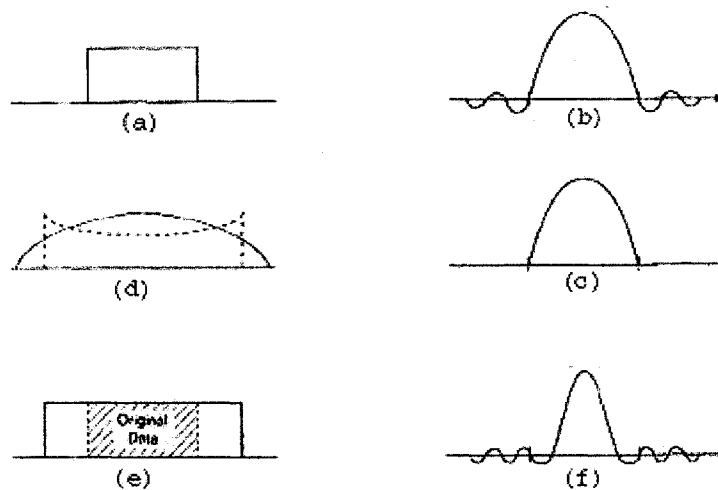
Figure 5.4 Super-SVA in one dimension:

(a) Input data (b) Fourier transform of input (c) SVA output (d) Inverse filter output
(e) Data replacement (f) Super-SVA output

The implementation of Super-SVA in two dimensional is a straightforward manner of the one dimension method. The Super-SVA procedure is applied to real MSTAR targets, and the results are shown in the below figures.
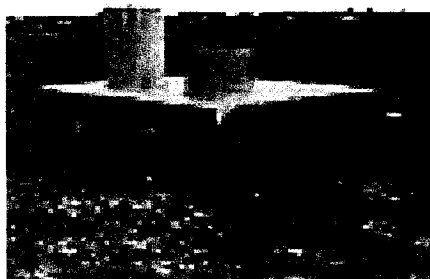
(a)
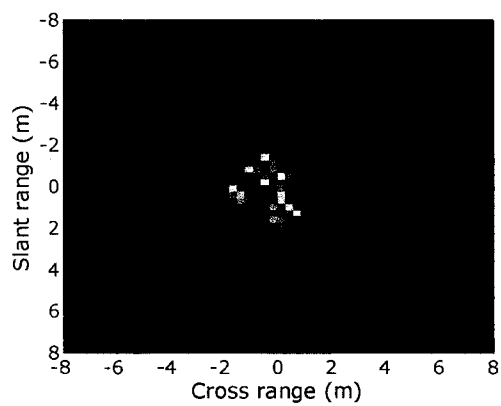
(b)
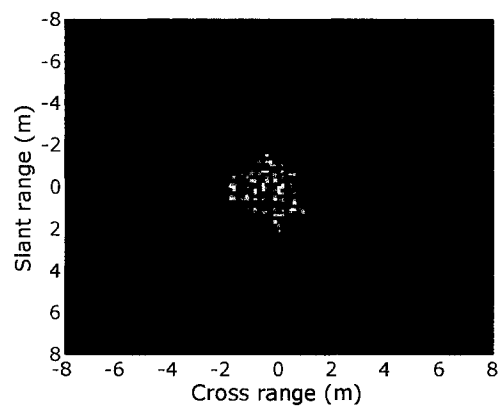
(c)

Figure 5.5 Super-SVA of MSTAR data 1:

(a) Original image (b) Super-SVA image

Super-SVA technique is applied to the original image obtained from the MSTAR data HB19377.015. The original MSTAR target is shown in Figure 5.6(a). And its corresponding rectangular windowed SAR image referred as original image is shown in Figure 5.6(b). The resulting super-SVA image is shown in Figure 5.6(c).

5.5 Observations

This chapter analyzed various extrapolation techniques. Papoulis extrapolation provides a practical solution to the extrapolation problem by minimizing the error energy. This minimum energy extrapolation method assumes that the known data is taken at positions of maximum energy and that the signal is narrow band signal. Minimum norm extrapolation techniques perform well for discrete signals but they are not widely employed in practical applications because of their computational complexity compared to the Papoulis method. Super-SVA technique involves SVA in the minimum energy extrapolation method. But this technique is not preferred for multiple or closely spaced targets because it is difficult to characterize an SVA image of distributed scatterers [28]. Hence the discussed extrapolation techniques are not common in real time applications.

CHAPTER 6

POLYNOMIAL WINDOWS

Over the last years, numerous investigators have proposed windows as different combinations of simple functions. The windows such as rectangular, Hann and Hamming are classical fixed windows in which the window length is the only parameter that controls the mainlobe width and the sidelobe level. Each window with its own characteristics is selected based on specific applications. There is no window called optimum, which can be used for all radar imaging applications.

Recently the theory of orthogonal polynomials has gained considerable attention in signal processing applications. The window functions that are derived from the orthogonal polynomials have interesting sidelobe roll-off properties; hence it can be used for better sidelobe apodization and SAR image enhancement. In this work a new window is constructed from the Jacobi orthogonal polynomials and applied in SAR imaging. This window has four parameters to control the window characteristics and hence expected to perform better than the existing windows. This is the first time a window is constructed from the Jacobi polynomials.

50

6.1 Welch Window

Welch is a simple window function that uses only polynomials and is also referred to as riesz window. The Welch window is defined as

$$w_{welch}(n) = 1 - \left| \frac{n}{N/2} \right|^2 , \quad |n| \le \frac{N}{2}$$ (34)

where N is the window length. It exhibits a discontinuous first derivative at the boundaries. The spectral characteristics of Welch window are plotted in Figure 6.1 for a window of length 31.
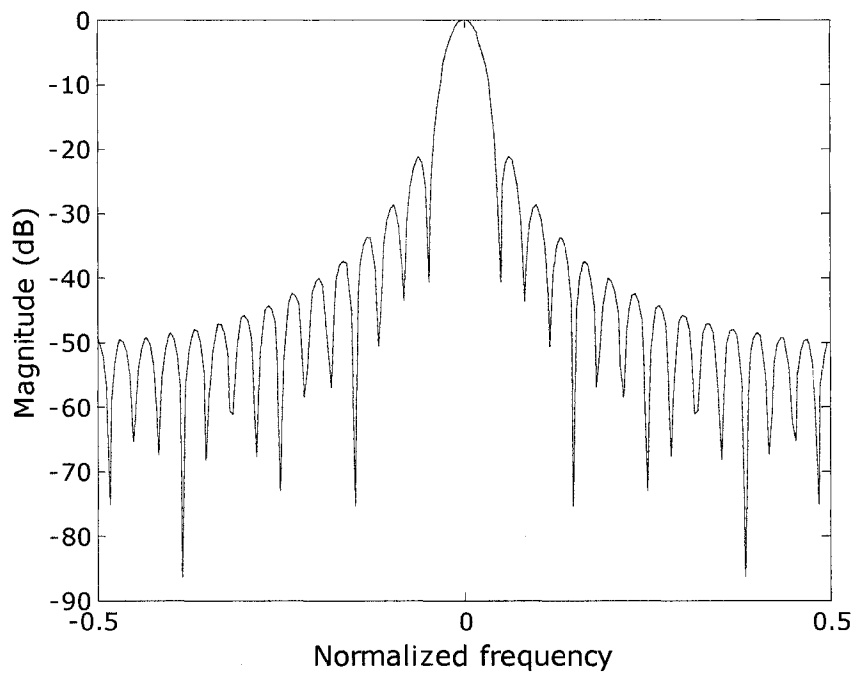
Figure 6.1 Spectral characteristics of Welch window

6.2 Dolph-Chebyshev Window

Dolph-Chebyshev [30-32] is a well-known classical window constructed from the Chebyshev polynomials for antenna and filter design applications. The Fourier transform of Chebyshev window is defined as

$$w(k) = \frac{T_{N-1}\left[x_0 \cos\left(\pi \frac{k}{N}\right)\right]}{T_{N-1}(x_0)} \quad 0 \le k \le N-1 \tag{35}$$

$$x_0 = \cosh\left(\frac{1}{N-1}\cosh^{-1}\frac{1}{r}\right) \tag{36}$$

where r is ripple ratio, and $T_{N-1}(x)$ is obtained through the recurrence relationship of Chebyshev polynomials. The Dolph–Chebyshev window is classified as adjustable window because it has two parameters window length and ripple ratio to control the spectral characteristics of the window. The time domain representation of the Chebyshev window [12] can be evaluated from the inverse Fourier transform:

$$w_n = \frac{1}{N}\left[T_{N-1}(x_0) + \sum_{i=1}^{(N-1)/2} T_{N-1}(x_0 \cos\frac{i\pi}{N})\cos(\frac{2n\pi i}{N})\right] \tag{37}$$

The Dolph-Chebyshev window is used to obtain minimum mainlobe width for a given ripple ratio. The important property of the Chebyshev window is that all the sidelobes have the same amplitude. Also the sidelobes of the Chebyshev window are highly sensitive to coefficient errors. These properties made the Chebyshev window unsuitable for many practical applications. In Figure 6.2 the spectral characteristics of the Chebyshev window are plotted for a window of length 31 and attenuation 30 dB.
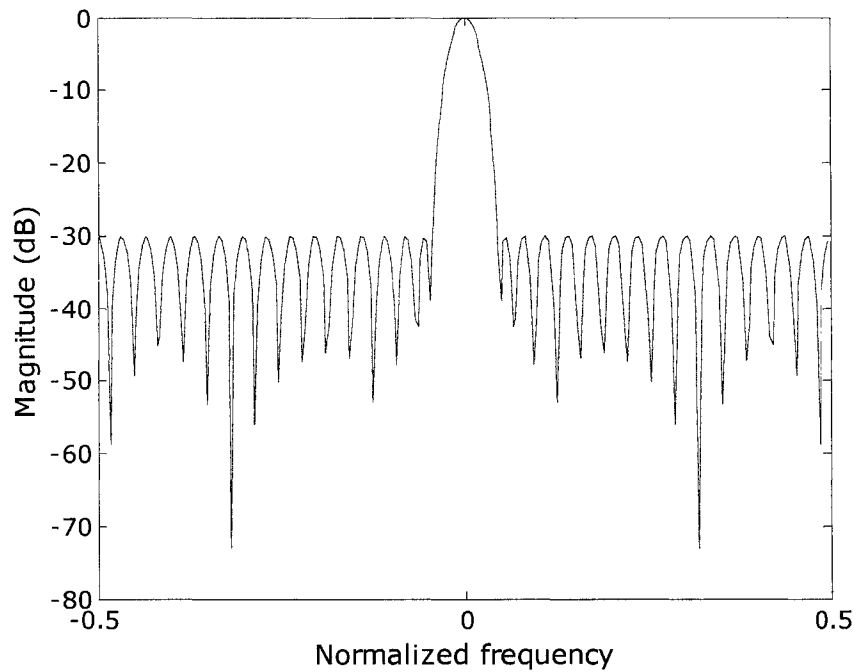
Figure 6.2 Spectral characteristics of Chebyshev window

6.3 Ultraspherical Window

Streit [33] used gegenbauer polynomial for antenna array approximation and observed that for a fixed mainlobe width, the Gegenbauer weights can achieve a dramatic decrease in sidelobes with small increase in the first sidelobe. Deczky [34] formed ultraspherical window based on Gegenbauer polynomials for digital filter design. The Ultraspherical window is given by

$$ w_n = \frac{1}{N}\left[C_{N-1}^{\alpha}(x_0) + \sum_{i=1}^{(N-1)/2} C_{N-1}^{\alpha}(x_0 \cos\frac{i\pi}{N})\cos(\frac{2n\pi i}{N}) \right] \tag{38} $$

where $C_{N-1}^{\alpha}(x_0)$ is calculated using the recurrence relationship of ultraspherical polynomials [35, 36], and x_0 is calculated similar to Chebyshev window for a given ripple ratio. The Ultraspherical window is also an adjustable window, which has three

parameters window length N , ripple ratio control x_0 , and sidelobe roll-off ratio α , to control the window characteristics. The third parameter, sidelobe roll-off ratio, helps to obtain desirable sidelobe pattern. Hence the ultraspherical window is more flexible than the Chebyshev window. Figure 6.3 plots the spectral characteristics of the ultraspherical window for different sidelobe roll-off ratio α , window length 31 and attenuation 50 dB. The increase in α reduces the sidelobe levels but increases the mainlobe width.
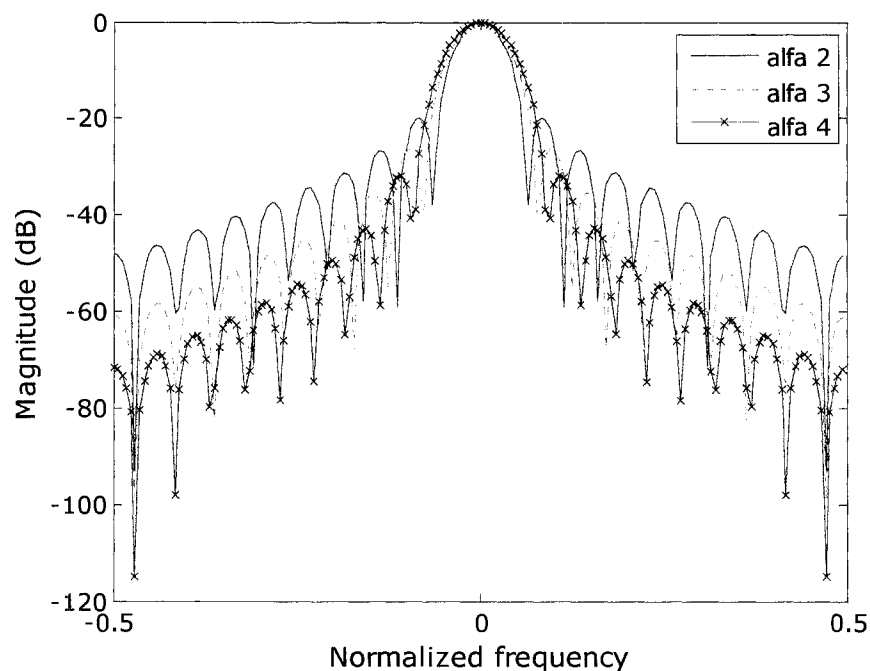
Figure 6.3 Spectral characteristics of ultraspherical window

6.4 Modified Legendre Window

Legendre window is also a special case of ultraspherical window, and it can be obtained by setting α to 0.5 in ultraspherical window. Modified Legendre window

proposed in [37] has the arbitrary parameter β to control the mainlobe width. The Legendre window is expressed as

$$w_n = \frac{1}{N}\left[P_N(x_0) + \sum_{i=1}^{(N-1)/2} P_{N-1}(x_0 \cos\frac{i\pi}{N})\cos(\frac{2n\pi i}{N})\right] \tag{39}$$

where $P_N(x)$ is calculated through the recurrence relationship of Legendre polynomials. In general, the initial values of Legendre polynomials are

$$P_0(x) = 1 \text{ and } P_1(x) = x. \tag{40}$$

In the modified Legendre window the parameter β is added to the $P_1(x)$. The value of x_0 is calculated similar to that of the Chebyshev window. The spectral characteristics of modified Legendre window for a window length 31, attenuation 30 dB and different β (beta 0.9, beta1 0.5, beta2 2) values are plotted in Figure 6.4. For higher β value the sidelobe decreases with the a little increase in the mainlobe width.
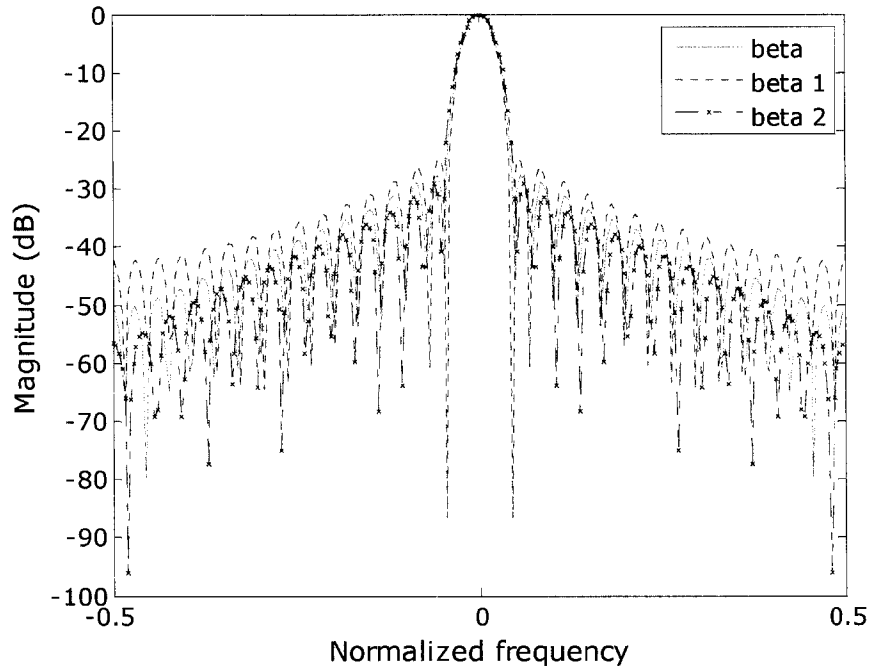
Figure 6.4 Spectral characteristics of Modified-Legender window

6.5 Jacobi Window

Chebyshev polynomials are a special case of Gegenbauer or ultraspherical polynomials, and the ultraspherical polynomials are a special case of Jacobi polynomials. Hence it is expected that the Jacobi polynomial window characteristics can be controlled better than that of the Chebyshev and Gegenbauer polynomials [38]. In this work, a new window is constructed based on the Jacobi polynomials and defined as

$$w_n = \frac{1}{N}\left[P_{N-1}^{\alpha,\beta}(x_0) + \sum_{i=1}^{(N-1)/2} P_{N-1}^{\alpha,\beta}(x_0 \cos\frac{i\pi}{N})\cos(\frac{2n\pi i}{N}) \right] \tag{41}$$

where $P_{N-1}^{\alpha,\beta}(x_0)$ is calculated from the recurrence relationship of Jacobi polynomials. The window characteristics of Jacobi polynomials are controlled by four parameters:

window length, ripple ratio, sidelobe roll-off ratios α and β. In Figure 6.5 the

spectral characteristics of Jacobi window for various α,β are plotted. The changes in

α,β values affect the first and second sidelobes without compromising mainlobe

width.
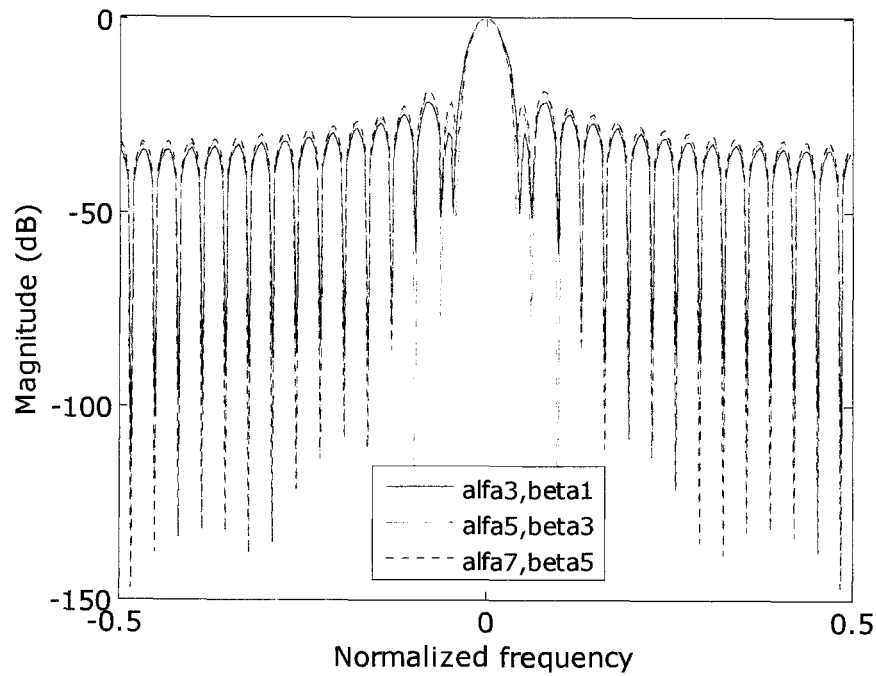
Figure 6.5 Spectral characteristics of Jacobi window

(a)

(b)

(c)
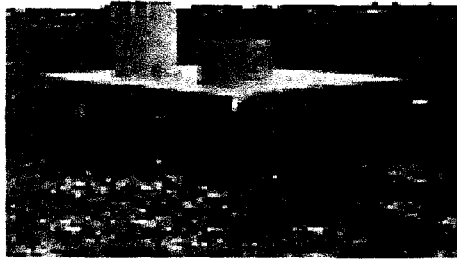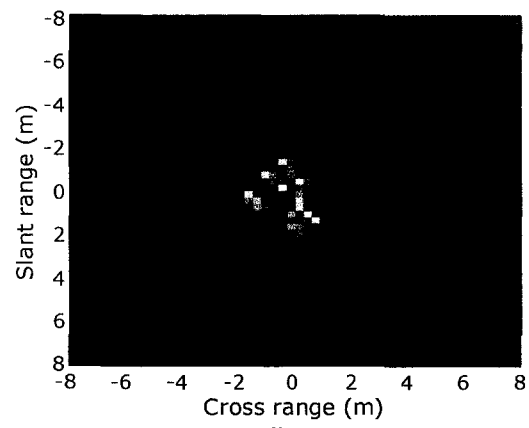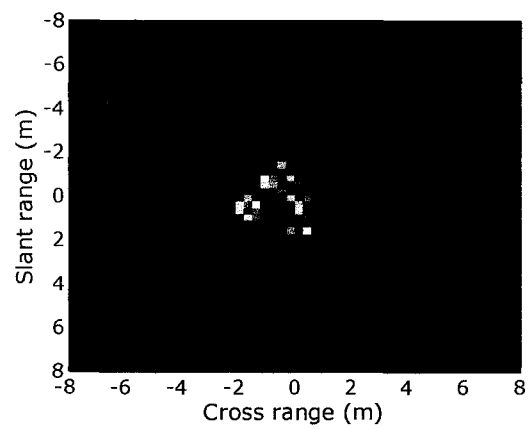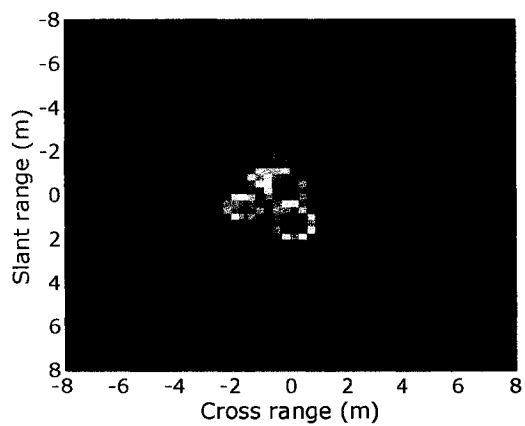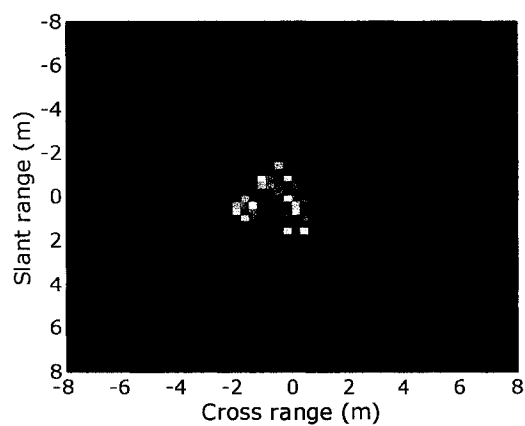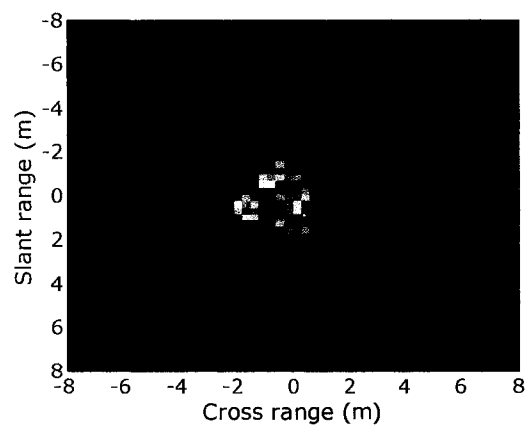
Figure 6.6 Polynomial windows in two dimensions:

(a) Slicy image (b) Reference image (c) Chebyshev image (d) Ultraspherical image
(e) Modified-Legender image (f) Jacobi image

The polynomial windows are applied to an image that is obtained from MSTAR data hb19377.015 and the resulting images are shown in Figure 6.6. Figure 6.6(a) shows the original Slicy image. The rectangular windowed image is considered as a reference image and shown in Figure 6.6(b). And Figures 6.6(c), 6.6(d), 6.6(e), and 6.6(f) show the Chebyshev, Ultraspherical, Modified Legendre, and Jacobi window images respectively. The Jacobi window images show the reduced sidelobe levels without compromisisng the mainlobe width compared to the other polynomial windows.

6.6 Discussion
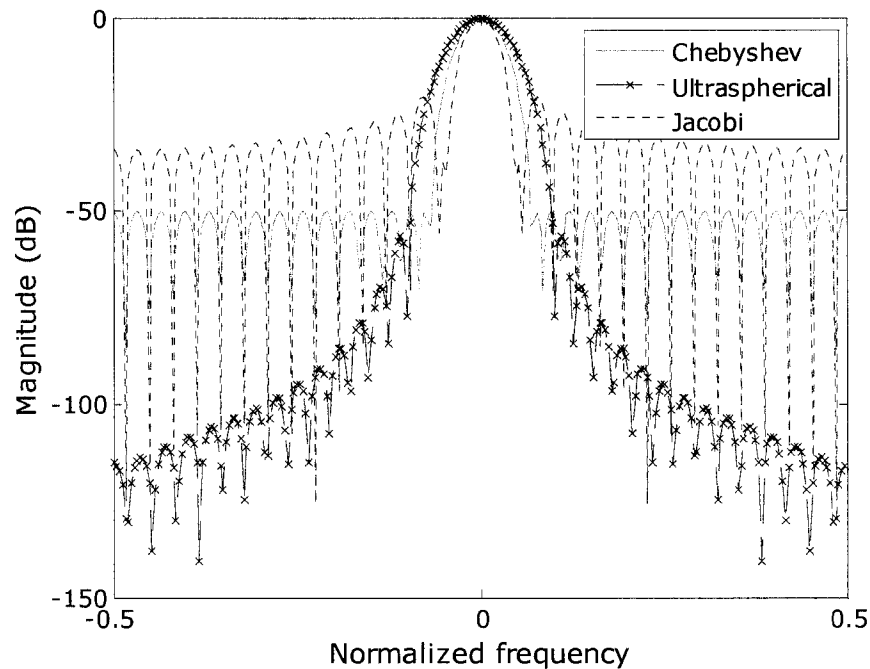
Figure 6.7 Comparison of Chebyshev, Ultraspherical, and Jacobi windows

The window characteristics of the discussed orthogonal polynomials are plotted in Figure 6.7 for a window of length 31 and attenuation 50 dB. The sidelobe roll-off ratio α is set to 5 to obtain the ultraspherical window characteristics. The values of α and β are set to 5 and 2 respectively for the Jacobi window. Among the polynomial windows, the Jacobi window has the narrowest mainlobe width. In the ultraspherical window, the increase in the sidelobe roll-off ratio affects the mainlobe width considerably than that of the Jacobi window. But the ultraspherical window has better trade off between mainlobe width and sidelobe levels among the discussed polynomial windows.
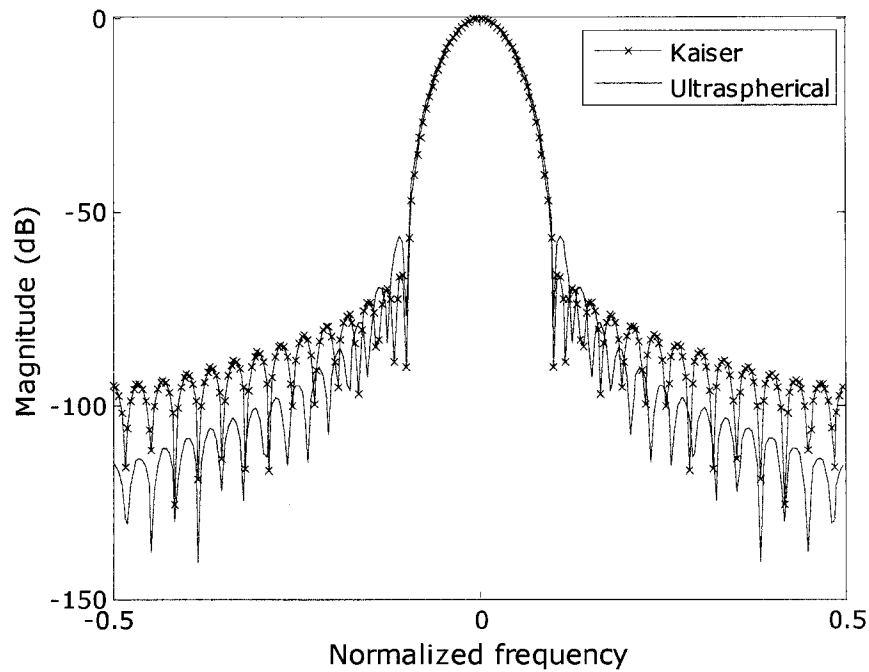
Figure 6.8 Comparison of Kaiser and Ultraspherical windows

The spectral characteristics of Kaiser and ultraspherical windows have better compromise between sidelobe levels and mainlobe width. In Figure 6.8 the spectral characteristics of both the apodizations are compared for a window length 31. For

ultraspherical window the sidelobe roll-off parameter α is set to 5, and attenuation to 50 dB.   In Kaiser window the parameter β is set to 9. Among these two apodizations, the ultraspherical window shows better performance.
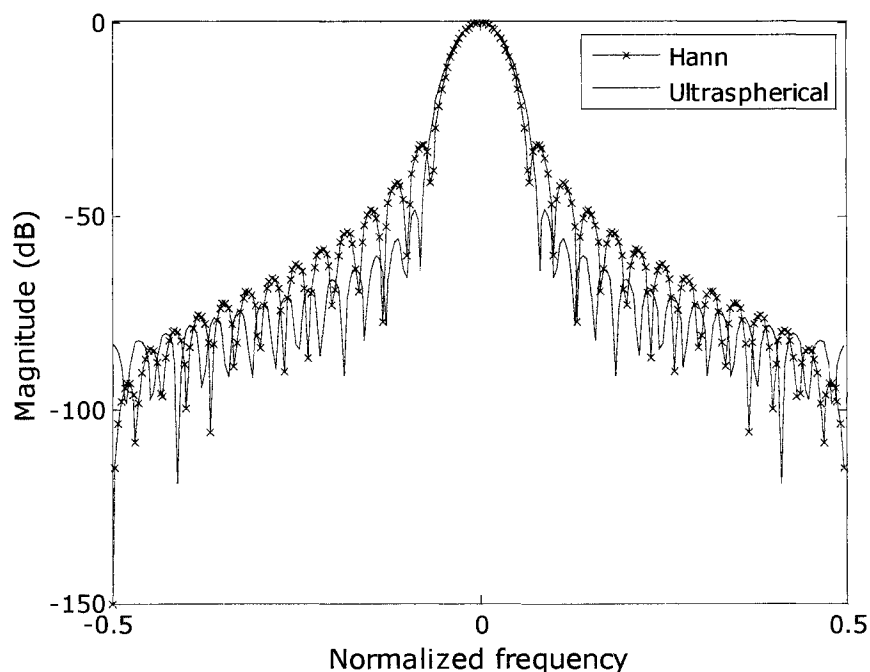
Figure 6.9 Comparison of Hann and Ultraspherical windows

Hann window has better window characteristics and widely applied in many practical applications. In Figure 6.9 the spectral characteristics of Hann and ultraspherical apodizations are plotted for a window length 31. For ultraspherical window the sidelobe roll-off parameter α is set to 2 and attenuation is set to 50 dB. Hann is a fixed window that depends only on its window length. The performance of ultraspherical window is better compared to the Hann window.

The rectangular window has the narrowest mainlobe width compared to the most of the discussed apodization functions. Jacobi window also has the narrowest mainlobe width like the rectangular window, and the sidelobe levels are suppressed

better than that of the rectangular window. Figure 6.10 shows the spectral characteristics of Jacobi and rectangular windows. The first sidelobe of the Jacobi window is suppressed very well than that of the rectangular window and the other sidelobe levels are also minimized compared to that of the rectangular apodization.
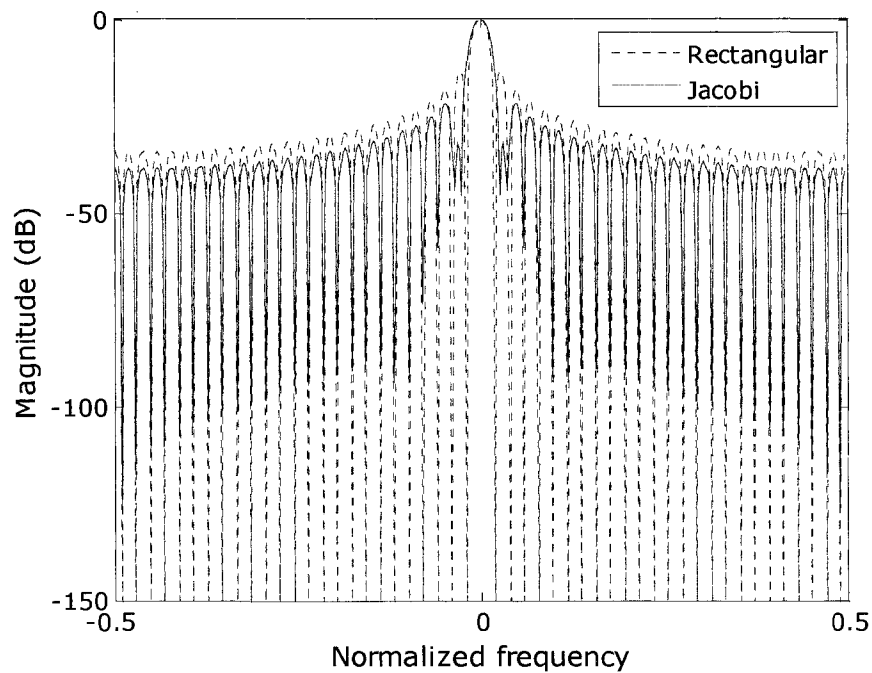
Figure 6.10 Comparison of rectangular and Jacobi windows

CHAPTER 7

SAR IMAGE ANALYSIS

In general, SAR system is evaluated based on functional and performance requirements with respect to the SAR imagery. Functional requirements are related to operational capabilities and the type of SAR imagery, and performance requirements are related to image quantity, image quality, and timeliness of the SAR imagery [4]. These performance requirements play a major role in the selection of SAR image processing algorithm, especially image quality requirements relative to scene size. This chapter briefly addresses the measurement of SAR image quality.

7.1 Image Quality Assessment

The typical measures of image quality that the SAR community uses are based on metrics like resolution, peak sidelobe level and integrated sidelobe level. These common SAR image quality parameters are obtained from the one dimensional impulse responses in both azimuth and range directions. In this work two dimensional windows are used enhance the SAR images. The two dimensional implementation of windows is a straight forward manner of one dimension windows. Hence the resolution and peak sidelobe levels are measured for the one dimensional window responses. Table 1 shows the one dimensional window characteristics for a window of length 31.

Table 1 Window Characteristics Comparison

Window	Peak sidelobe level dB	Resolution 3dB (Normalized frequency bins)	P.S.L/L.S.L
Rectangle	-13	0.031	13/30
Hann	-32	0.048	32/93
Kaiser($\beta = 9$)	-66.5	0.06	66.5/95
Filler	-50	0.06	50/115
Norton_Beer	-17	0.034	17/34
Chebyshev	-30	0.05	30/30
Ultraspherical $\begin{pmatrix} \alpha = 4 \\ \alpha = 5 \end{pmatrix}$	-32 -56	0.073 0.061	32/70 56/115
Jacobi $(\alpha = 3, \beta = 1)$ Jacobi $(\alpha = 3, \beta = 1)$	-23.5(FSL), -22.5 -30(FSL), -23.5	0.035 0.036	22.5/34 23.5/35

Table 1 shows resolution, peak sidelobe level, resolution and ratio of highest to lowest sidelobe levels (PSL/LSL) of the discussed windows. The Jacobi window has reasonably narrow mainlobe width among the polynomial windows. It also has better sidelobe apodization than the rectangular and Norton-Beer windows that have almost the same narrow mainlobe width.

Degraff [26] discussed the SAR image analysis based on estimation theory concepts such as mean and variance. Table 2 shows the mean and standard deviation values of a various windowed simulated single point target.

Table 2 Statistical values comparison of simulated target

Simulated Target	Mean	Standard Deviation
Original target	1.2805	1.1807
Hann	0.4902	0.4563
Kaiser	0.3836	0.3367
$\text{Chebyshev}\begin{pmatrix} 30\,dB \\ 50\,dB \end{pmatrix}$	0.6743 0.4897	0.6032 0.4323
Ultraspherical	0.3488	0.2984
Jacobi	0.7205	0.6472
Filler(α=0.3)	0.3810	0.3311
Norton-Beer	0.9262	0.8465

The mean values in Table 2 show the dispersion of image intensity values. In some cases, the standard deviation helps to measure the noise reduction. In Table 2, the standard deviation value of the original target is higher compared to the other windowed values. The Chebyshev window provides low standard deviation for 50 dB attenuation than the 30 dB attenuation. The Jacobi window has lower standard deviation value than the Filler and rectangular windows.SVA technique is used in many SAR imaging applications because of its better sidelobe reduction. The Filler,

Kaiser, and Ultraspherical windows have almost the same and lower standard deviation values than the other windows.

Table 3 Statistical values comparison of SAR image

MSTAR target SLICY	Mean value	Standard deviation
Original target image	0.0603	0.1986
Hann window image	0.0304	0.1171
Kaiser window image	0.0264	0.0965
Chebyshev $\begin{pmatrix} 30\,dB \\ 50\,dB \end{pmatrix}$	0.0372 0.0307	0.1424 0.1188
Ultraspherical	0.0225	0.0764
Jacobi	0.2991	0.1149
Filler(α=0.3)	0.0255	0.0914
Norton-Beer	0.0483	0.1742

In Table 3 the mean and standard deviation values of MSTAR target Slicy is shown for different apodization techniques. The standard deviation values of the windowed SAR images vary similar to that of the windowed simulated target standard deviation values in Table 2. Hence it is assumed that the Jacobi window has better noise reduction than the rectangular and Norton-Beer windows. Because the image quality is a subjective notion [39], it is difficult to analyze the image quality with the estimation theory concepts discussed above. Several SAR image quality assessments are reported in various literatures [40, 41]. In future a better SAR image quality assessment will be developed.

CHAPTER 8

CONCLUSIONS AND FUTURE WORK

In this work, a new window is constructed from the Jacobi orthogonal polynomials and the results show that the Jacobi window has reasonably narrow mainlobe width, which is essential for good image resolution. The other orthogonal polynomial windows such as Chebyshev, Legendre, and Ultraspherical can be obtained by setting specific values to the Jacobi window arbitrary parameters α and β.

The Filler, Kaiser, and Ultraspherical windows have almost the same spectral characteristics. Hence the Filler and Kaiser windows can be obtained from the Jacobi window by selecting proper Jacobi window parameters. The Jacobi window is applied to SAR imaging for the first time, and the analyzed results show better resolution. Even though sidelobe reduction of the Jacobi window is less compared to the commonly used windows such as Kaiser and Hann, the results show that the proper selection of Jacobi window parameters will provide promising results in the future.

In polynomial windows the window length is related to the polynomial order, and causes implementation difficulties in SAR imaging applications when the image size is large. This problem will be avoided in the future by applying moving polynomial windows technique. Also an adaptive window that gives optimum window characteristics will be obtained by combining the discussed polynomial windows.

68

REFERENCES

1. Mehrada Somekh, Synthetic Aperture Radar Signal Processing with MATLAB Algorithms, Wiley-Interscience Publication, 1996.

2. Imaging Radar, NASA Website: http://southport.jpl.nasa.gov/.

3. Sandia National Laboratories website: www.sandia.gov/.

4. W. G. Carrara, R. S. Goodman, R. M. Majewski, Spotlight Synthetic Aperture Radar Signal Processing Algorithms, Artech House, 1995.

5. Jae-Sok Son, G. Thomas, B. C. Flores, Range-Doppler Radar Imaging and Motion Compensation, Artech House, 2001.

6. Ricardo Radaelli-Sanchez and Richard Baraniuk, "Gibbs's Phenomenon," at http://cnx.rics.edu/content/m10092/latest.

7. F. J. Harris, "On the use of windows for harmonic analysis with discrete Fourier Transform," Proceedings of the IEEE, vol. 66, no. 1, January 1978.

8. H. Nuttall, "Some Windows with Very Good Sidelobe Behaviour," IEEE Transactions on Acoustics, speech, and signal processing, Vol. ASSP-29, no. 1, February 1981.

9. G. Thomas, J. Sok-Son, B. C. Flores, "Sidelobe Apodization using parametric windows," SPIE Proc Algorithms for Synthetic Aperture Radar Imagery VI, vol. 3721, April 1999.

10. G. Thomas, B. C. Flores, J. Sok-Son, "SAR Sidelobe Apodization Using The Kaiser Window," IEEE International conference on Image Processing, September 2000, vol. 1, pp. 709-712.

11. M. K. Tahic and D. A. Naylor, "Apodization Functions for Fourier Transform Spectroscopy," OSA 2005.

12. A. S. Filler, "Apodization and Interpolation in Fourier Transform Spectroscopy," J. Opt. Soc. Am, vol. 54, no. 6, June 1964.

13. R. H. Norton and R. Beer, "New apodizing functions for Fourier Spectrometery," J. Opt. Soc. Am, vol. 66, no. 3, March 1976.

14. E. Anterrieu, P. Waldteufel, A. Lannes, "Apodization functions for 2-D hexagonally sampled synthetic aperture imaging radiometers," IEEE Transactions on Geoscience and Remote Sensing, vol. 40, no. 12, December 2002, pp: 2531-2542.

15. H. C. Stankwitz, R. J. Dallaire, J. R. Fienup, "Spatially Variant Apodization For Sidelobe Control In SAR Imagery," Proc. of IEEE Radar Conference, March 1994, pp. 132 – 137.

16. H. C. Stankwitz, R. J. Dallaire, J. R. Fienup, "Nonlinear apodization for sidelobe control in SAR imagery," IEEE Trans. on Aerospace and Electronic Systems, vol. 31, no. 1, January 1995.

17. Ji Huibo, Wang Yiding, Wu Yirong, Hong Jan, "A modified apodization method in SAR/ISAR processing," IEEE Proc. of Geoscience and Remote Sensing Symposium, vol. 6, July 2003, pp: 3991-3994.

18. J. Sok-Son, "Magnitude difference based SAR/ISAR sidelobe reduction and image resolution enhancement method," September 2004.

19. Sensor data management system website: https://www.sdms.afrl.af.mil/.

20. http://www.alphatech.com/secondary/techpro/projects/mstar/MSTAR_Top_Level.html

21. B. R. Hunt, "Super-Resolution of Imagery: Understanding the basis for recovery of spatial frequencies beyond the diffraction limit," IEEE Proc. of Information, Decision, and Control, February 1999, pp. 243-248.

22. Papoulis, "A new algorithm in spectral analysis and band-limited signal extrapolation," IEEE Transanctions on Cirucits and Systems, vol. 22, pp. 735-742, September 1975.

23. R. W. Gerchberg, "Super-resolution through error energy reduction," Optica Acta, vol. 21, no. 9, pp. 709-720, 1974.

24. M. Sabri and W. Steenaart, "An approach to band-limited signal extrapolation: The extrapolation matrix," IEEE Transactions on Circuits and Systems, vol.25, pp. 74-78, February 1978.

25. Jain, S. Ranganath, "Extrapolation algorithms for discrete signals with application in spectral estimation," IEEE Transactions on Acoustics, speech, and signal Processing, vol. 29, no. 4, August 1981, pp. 830-845.

26. S. Cabraera and T. Parks, "Extrapolation and spectral estimation with iterative weighted norm modification," IEEE Transactions on Signal Processing, vol. 39, pp. 842-851, April 1991.

27. H. C. Stankwitz, M.R. Kosek, "Sparse aperture fill for SAR using Super-SVA," Proc. of IEEE Radar Conference, May 1996, pp.70-75.

28. S. R. Degraff, "SAR Imaging via modern 2-D spectral estimation methods," IEEE Transactions on Image Processing, vol. 7, no. 5, May 1998, pp.729-761.

29.   Xiaojian Xu, R. M. Narayanan, "SAR image enhancement using non-integer Nyquist SVA technique," IEEE International Symposium on Antennas and Propagation, vol. 4, June 2002, pp. 298 - 301.

30.   C. L. Dolph, "A current distribution for broadside arrays which optimizes the   relationship between beamwidth and side-lobe level," Proc. of IRE, vol. 34, pp. 335-348, June 1946.

31.   Antoniou. A, Digital Filters: Analysis, Design, and Applications, 1993, Second Edition McGraw-Hill, 686 pp.

32.   Lynch, Peter, "The Dolph-Chebyshev Window: A Simple Optimal Filter," 1997, American Meteorological Society, Available Online.

33.   R. L. Streit, "A two parameter family of weights for non-recursive digital filters and antennas," IEEE Transactions on Acoustics, speech, and signal processing, vol. 32, no. 1, pp. 108-118, February 1984.

34.   G. Deckzy, "Unispherical windows," IEEE International Symposium on Circuit and Systems, vol. 2, pp. 85-88, May 2001.

35.   M. Abramowitz and I.A. Stegun, Handbook of Mathematical Functions, Nation Bureau of Standard Applied Mathematics Series, 1965.

36.   S. W. A. Bergen, A. Antoniou, "Design of ultraspherical windows with prescribed spectral characteristics," Proc. of the IEEE International Symposium on Circuits and Systems, vol. 4, pp. 169 -172, May 2003.

37.   M. Jaskula, "New windows family based on modified Legendre polynomials," IEEE Instrumentation and Measurement Technology Conference, May 2002, vol. 1, pp: 553-556.

38. R. Devarajulu, Jae Sok Son, "Orthogonal Polynomials in SAR Imaging," 1009th AMS meeting, Oct. 2005 will be found in vol. 26, issue 4 of Abstracts of papers presented to the American Mathematical Society.

39. R. M. Rangayyan, Biomedical Image Analysis, CRC Press, 2005.

40. A. freeman, "SAR Calibration: An Overview," IEEE transactions on Geoscience and Remote sensing, vol. 30, no. 6, November 1992.

41. M. Rossi, B. Rogron, and D. Massonnet, "JERS-1 SAR Image Quality and Interferometric Potential," IEEE transactions on Geoscience and Remote sensing, vol. 34, no. 3, May 1996.

42. B. H. Smith, "Generalization of Spatially Variant Apodization Noninteger Nyquist Sampling rates," IEEE Transactions on Image Processing, vol. 9, no. 6, June 2000.

APPENDICES

Data Manipulation

The data's used in this work were collected by Sandia National Laboratory SAR sensor platform in 1995 at the Redstone Arsenal, Huntsville, AL. This data collection was supported by DARPA and Air Force Research as a part of moving and stationary target acquisition and recognition program. Hence these data's are referred to as MSTAR data sets.

MSTAR Target data sets of targets Slicy and T-72 battle tank, and MSTAR clutter data set of a target rural and urban scene of Huntsville are selected for this research work. Each data file is constructed with a Phoenix formatted (ASCII) header which contains detailed ground truth and sensor information, and a data block that is written in Sun floating point format and is divided into two blocks, a magnitude block followed by a phase block. These data sets were converted to image display format with the help of MSTAR and Phoenix conversion tools available in the sensor data management system. These conversion tools have programs in C and MATLAB that help to extract the magnitude and phase data display format. An example of a Phoenix header attached to a MSTAR data set is shown below:

74

[PhoenixHeaderVer01.04]

PhoenixHeaderLength= 01569

PhoenixSigSize= 10549089

[PhoenixHeaderVer01.04]

PhoenixHeaderLength= 01569

PhoenixSigSize= 10549089

PhoenixSigNum= 0001

PhoenixHeaderCallingSequence=

HeaderVersionNumber= 3KM

native_header_length= 512

Filename= hb06158

Image_MD5_CheckSum= 25ba3fc4d3003b6a98283f91515480bf

NumberOfColumns= 1478

NumberOfRows= 1784

Site= huntsville_al

DesiredDepression= 15

DesiredGroundPlaneSquint= -90

DesiredSlantPlaneSquint= -90

DesiredRange= 4500

MeasuredDepression= 15.078125

MeasuredGroundPlaneSquint= -90.218460

MeasuredSlantPlaneSquint= -90.210938

MeasuredRange= 4470

MeasuredAimpointLatitude= 34.790459

MeasuredAimpointLongitude= 273.254486

MeasuredAimpointElevation= 186.942993

MeasuredAimpointLatitudeReference= N

MeasuredAimpointLongitudeReference= E

MeasuredAntennaLatitude= 34.828766

MeasuredAntennaLongitude= -86.737328

MeasuredAircraftHeading= -79.773438

MeasuredAircraftAltitude= 1349.750000

RadarMode= mode 4 - strip map

SensorCalibrationFactor= 42.995998

RadarPosition= bottom

SceneCenterReferenceLine= 280

X_Velocity= 57.152344

DataCollecters= Sandia National Lab

CollectionDate= 19950905

CollectionTime= 081903

CollectionName= hb

SensorName= Twin Otter

Classification= UNCLASSIFIED

MultiplicativeNoise= -10 dB

AdditiveNoise= -32 to -34 dB

CenterFrequency= 9.60 GHz

CrossRangeWeighting= -35dB_Taylor

RangeWeighting= -35dB_Taylor

DynamicRange= 64 dB

Bandwidth = 0.591 GHz

AzimuthBeamwidth= 8.8 Degrees

ElevationBeamwidth= 6.8 Degrees

RangeResolution= 0.304700

CrossRangeResolution= 0.304700

RangePixelSpacing= 0.202148

CrossRangePixelSpacing= 0.203125

Polarization= HH

[EndofPhoenixHeader]

The PhoenixHeader shows that the MSTAR datasets are Taylor windowed. In this research the unwindowing process is applied after data manipulation before forming SAR image. The below is the original image of a MSTAR clutter data HB06158 that shows a rural and urban scene of Huntsville, Alabama.
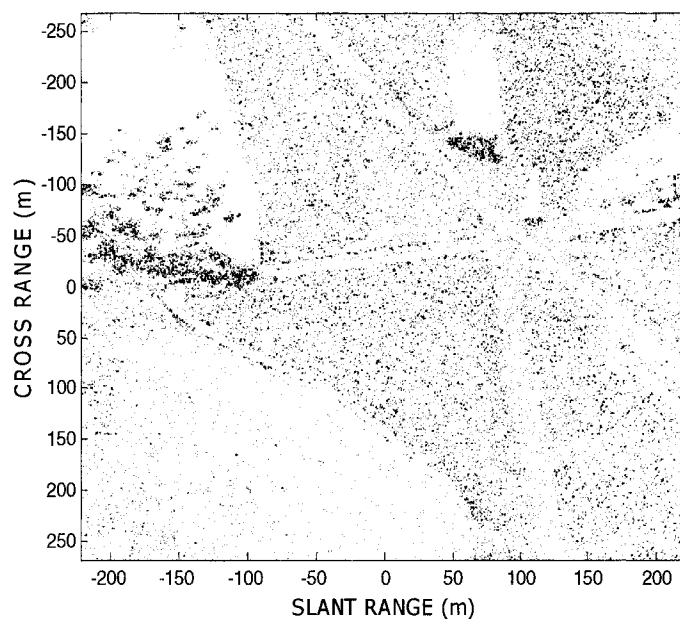

Figure A.1 Huntsville rural scene image